Journal of Sound and Vibration 362 (2016) 252–275

Contents lists available at ScienceDirect

Journal of Sound and Vibration

journal homepage: www.elsevier.com/locate/jsvi

On sound scattering by rigid edges and wedges in a flow, with applications to high-lift device aeroacoustics

Michel Roger [a,1], Stéphane Moreau [b,*,2], Korcan Kucukcoskun [c,3]

[a] *École Centrale de Lyon, 69134 Écully, France*
[b] *Université de Sherbrooke, Département de génie mécanique, Sherbrooke, QC, Canada J1K2R1*
[c] *École Centrale de Lyon, 69134 Écully, France*

A R T I C L E I N F O

Article history:
Received 2 March 2015
Received in revised form
1 October 2015
Accepted 5 October 2015
Handling Editor: Y. Auregan
Available online 23 October 2015

Keywords:
Aeroacoustics
High-lift Devices
Analytical Modeling

A B S T R A C T

Exact analytical solutions for the scattering of sound by the edge of a rigid half-plane and by a rigid corner in the presence of a uniform flow are considered in this work, for arbitrary source and observer locations. Exact Green's functions for the Helmholtz equation are first reviewed and implemented in a quiescent propagation space from reference expressions of the literature. The effect of uniform fluid motion is introduced in a second step and the properties of the field are discussed for point dipoles and quadrupoles. The asymptotic regime of a source close to the scattering edge/wedge and of an observer far from it in terms of acoustic wavelengths is derived in both cases. Its validity limits are assessed by comparing with the exact solutions. Typically the asymptotic directivity is imposed by Green's function but not by the source itself. This behaviour is associated with a strong enhancement of the radiation with respect to what the source would produce in free field. The amplification depends on the geometry, on the source type and on the source distance to the edge/wedge. Various applications in aeroacoustics of wall-bounded flows are addressed, more specifically dealing with high-lift device noise mechanisms, such as trailing-edge or flap side-edge noise. The asymptotic developments are used to highlight trends that are believed to play a role in airframe noise.

1. Introduction

The role of solid surfaces in aeroacoustics is twofold. Firstly they participate in the generation of sound by direct interaction with flows. Secondly they redistribute the sound radiated by sources possibly located elsewhere. In that sense they act as either sources of sound or scattering obstacles and can be artificially classified as active or passive surfaces, respectively. The physical understanding and the modeling of both aspects are key issues in the definition of noise reduction strategies in many engineering applications. Pure sound scattering is usually investigated using the classical theory of diffraction in linear acoustics. Aerodynamic sound production in the presence of solid surfaces can be formulated from the standpoint of linear acoustics by resorting to the acoustic analogy. According to Lighthill's original statement [1] and related

* Corresponding author.
E-mail addresses: michel.roger@ec-lyon.fr (M. Roger), stephane.moreau@usherbrooke.ca (S. Moreau).
[1] Laboratoire de M'ecanique des Fluides et Acoustique.
[2] D´epartement de G´enie M´ecanique.
[3] Current position in Siemens Industry Software.

http://dx.doi.org/10.1016/j.jsv.2015.10.004
0022-460X/

Nomenclature

Italic symbols

A_0	Kutta-correction factor
c	chord length
c_0	speed of sound
D	directivity factor
E	Fresnel integral
F	complex function for the 2D half-plane Green's function
$\mathbf{F}$	dipole strength vector
G	Green's functions for the Helmholtz equation
G_K	correction to Green's function for the Kutta condition
G_{M_0}	Green's functions with uniform flow
G_∞	2D asymptotic Green's function in free field
h	flap side-edge thickness
H	Heaviside function
$J_\nu, H_\nu^{(1)}$	Bessel and Hankel functions of the first kind
$k=\omega/c_0$	acoustic wavenumber
$K=k/\beta$	modified wavenumber
k_1^*	dimensionless aerodynamic wavenumber
K_n	modified Bessel functions
ℓ	unsteady lift on a flap
$l_{\max}$	size of quadrilateral elements
M_0	Mach number
p	acoustic pressure
P	dipole strength
P_ν^μ	general Legendre functions
q	monopole strength
$\mathbf{Q}$	quadrupole strength tensor
$(\overline{r},\overline{\theta},z)$	corrected observer cylindrical coordinates
$(\overline{r}_0,\overline{\theta}_0,z_0)$	corrected source cylindrical coordinates
$r_> = \max(\hat{r},\hat{r}_0)$	maximum distance
$r_< = \min(\hat{r},\hat{r}_0)$	minimum distance
$\overline{r}$, $\overline{r}_{1,2}$, $\overline{r}_{1,2}$	corrected 3D and 2D scattering distances
$S_{1,2}$, $s_{1,2}$	3D and 2D integral bounds in convected Green's functions
S_0	convection-corrected distance
$T_{i,j}$	quadrupole strength components
U_0	flow speed
$\mathbf{x}=(x,y,z)$	observer Cartesian coordinates for an edge
$\mathbf{x}_0=(x_0,y_0,z_0)$	source Cartesian coordinates for an edge
$\mathbf{x}=(r,\theta,z)$	cylindrical observer coordinates for an edge
$\mathbf{x}_0=(r_0,\theta_0,z_0)$	cylindrical source coordinates for an edge
$\mathbf{x}=(x_1,x_2,x_3)$	observer Cartesian coordinates for a corner
$\mathbf{x}_0=(y_1,y_2,y_3)$	source Cartesian coordinates for a corner
$\mathbf{x}=(\hat{r},\Theta,\phi)$	observer spherical coordinates for a corner
$\mathbf{x}_0=(\hat{r}_0,\Theta_0,\phi_0)$	source spherical coordinates for a corner
$X_0, X=x_0/\beta, x/\beta$	modified streamwise coordinates for an edge
$X_1, Y_1=x_1/\beta, y_1/\beta$	modified streamwise coordinates for a corner

Greek symbols

α_d	dipole inclination angle
$\beta=\sqrt{1-M_0^2}$	compressibility parameter
ε_m	constant in Green's function for rigid wedge
$\overline{\theta}_1$	angle in the correction to Green's function for the Kutta condition
$\overline{\theta}_0, \overline{\theta}$	corrected spherical source and observer angles
λ	acoustic wavelength
ϕ^{2D}, ϕ^{3D}	two-or three-dimensional acoustic potentials
Φ	wedge aperture angle
φ	projection angle for the half-plane Green's function
ρ_0	fluid density
ω	angular frequency

Subscripts/superscripts symbols

κ, m	summation indices
K	Kutta-condition correction
M_0	flow-corrected quantity
$(1/2)$	half-plane

works by Howe [2] and Ffowcs Williams and Hall [3], for instance, unsteady flow patterns interacting with solid surfaces can be interpreted as equivalent quadrupoles distributed in the fluid, the direct sound of which is scattered by the surfaces. This view is developed in some asymptotic theories of high-lift device noise [4,5]. According to Ffowcs Williams and Hawkings' statement of the analogy [6], surfaces explicitly involved in noise generation can also be mathematically interpreted as equivalent sources of lower orders. *A priori* the latter point of view is well suited for active surfaces and the former for passive surfaces. But the distinction is questionable when two bodies in close vicinity of each other are embedded in a disturbed flow region. The present analysis is dedicated to the high-lift devices that are deployed when the wing of an aircraft operates in approach and landing conditions. The source and scattering surfaces are implicitly assumed to be well separated, which only covers a part of the complete physics in most cases of interest. For instance a deployed flap (Fig. 1) can be interpreted as a distribution of equivalent sources, the sound of which is scattered by the main part of the wing. The underlying mechanism partly contributes to the airframe noise that also includes landing-gear associated sources. Airframe noise in itself is recognized as a major contributor to the total noise of an aircraft at approach, essentially because the modern high by-pass ratio engines are much quieter at idle power.

Going into the details, High-Lift Device (HLD) noise involves distributed sources along the leading or trailing edges of the wing ((2) in Fig. 1), the slat and the flap ((1) and (4) in Fig. 1), as well as sources that concentrate around the span ends of wing elements such as flap side-edges ((3) in Fig. 1) or slat corners. In the present study two contributions in which sound

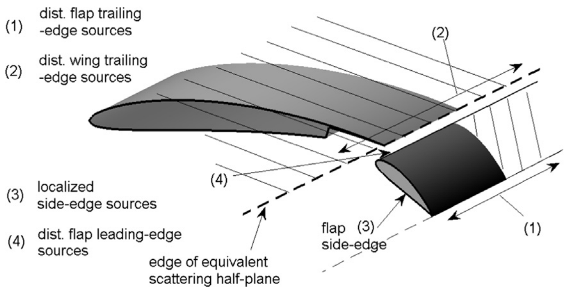

Fig. 1. High-lift device architecture including a wing and a trailing-edge flap (no leading-edge slat). Breakdown of areas of aerodynamic sound generation. Sources (1) and (2) are not addressed in the present work. Flap leading-edge sources (4) addressed in Section 2.5; flap side-edge sources (3) addressed in Section 3.

scattering is a key mechanism are addressed. One arises from the spanwise-distributed sources induced on a flap leading edge by impinging vortical disturbances produced in the wing-flap gap ((4) in Fig. 1). The other one is associated with the initial high-frequency oscillations of the detaching shear layers from flap side-edge corners; it is only a part of the roll-up that leads to the side-edge vortex. In the first case the mean flow parameters do not vary significantly in the spanwise direction. The sound sources have two-dimensional features, even though they radiate in a three-dimensional space. In the second case the strong three-dimensional character of the flow responsible for the sound production makes the investigation of the mechanism more challenging with analytical means. Yet the analytical approach is chosen in the present work to point out some features of interest.

The prediction of HLD noise generation and radiation can also be achieved by numerical methods. The high Reynolds numbers of these devices (greater than 10^6 based on a typical chord length) however still preclude using full compressible Direct Numerical Simulation (DNS) or Large Eddy Simulation (LES) methodology to yield the acoustic field directly. A hybrid technique coupling the determination of the sources by an unsteady compressible simulation and a propagation technique is applied instead. Unsteady Reynolds-Averaged Navier–Stokes (RANS) computations were first used by Khorrami et al. [7,8]. RANS coupled with Linearized Euler Equations (LEE) and RANS/LES methodologies were later applied by Terracol et al. [9] and Deck et al. [10] respectively. More recently König et al. proposed a hybrid methodology combining LES and linearized equations [11]. Finally the first complete direct noise simulation of a high-lift device was achieved by Satti et al. with a Lattice Boltzmann Method [12].

Numerical approaches have the advantage of accounting for the exact geometry, though they usually consider a limited span and often still ignore details that might contribute to the sound generation such as slat tracks, de-icing vents and flap track fairings. They reproduce realistic flow features, but are very demanding in terms of computational resources. Alternatively, analytical investigations have some mathematical interest and provide fast-running approximate predictions at the price of drastic assumptions. Even though the underlying geometrical simplifications may be a shortcoming, the simplicity of the solution provides key insight into the scattering mechanisms. Furthermore exact analytical solutions in simple configurations are also a reference for the validation of numerical techniques that can be applied next to more complicated ones.

From the methodological standpoint the present work is addressing model problems that can be solved analytically based on the use of exact tailored Green's functions. Geometrical configurations for which such Green's functions are known are very few in the mathematical theory of waves. Nevertheless a wide class of them can be generated by associating two half-planes sharing the same edge and featuring a wedge. The wedge angle Φ is defined as the aperture angle of the available propagation space. If Φ is an acute angle such that π/Φ is an integer, the method of images provides the exact solution [13]. The half-space bounded by an infinite plane and the quarter of space bounded by two perpendicular half-planes are just classical special cases of the method ($\Phi=\pi$ and $\Phi=\pi/2$, respectively). More general configurations and especially wedges of obtuse aperture angles require more sophisticated theoretical developments. The present paper is dealing with two particular analytical expressions of Green's function. One is for a rigid corner, corresponding to the special, non-integer value $\pi/\Phi=2/3$. It is suited to the analysis of some asymptotic aspects of flap side-edge noise. The other one is for a rigid half-plane and corresponds to $\pi/\Phi=1/2$. It is used for instance to describe the scattering by the trailing edge of a wing. Both are based on general formulations derived by MacDonald [14] for arbitrary source and observer locations in a medium a rest.

Because the exact expressions of Green's functions are rather complicated and require numerical implementation, they have been seldom used as such. Most applications in acoustics and aeroacoustics only resort to asymptotic expansions [13,3]. Indeed for some declinations of the generic configurations the observer is in the acoustic far field ensured by the condition $kR \gg 1$, where $k=\omega/c_0$ is the acoustic wavenumber and R is the source-to-observer distance, and the source is at a very short normal distance r_0 from the edge/wedge, so that $kr_0 \ll 1$. This asymptotic regime justifies approximations that lead to simplified, closed-form solutions. Now comparing exact and asymptotic formulations appears as the only way of assessing the validity range of the latter. Furthermore in many cases the full expression of Green's function is required, and the function itself must be extended to account for the presence of flow so that flight effect is included in the analysis. This motivated the authors for implementing the exact expressions of Green's functions with flow and applying them to infer important features of the sound radiation.

The sound scattering by a rigid half-plane in the presence of a uniform flow is first addressed in Section 2, in the case of a trailing edge. The sound field of point dipoles and quadrupoles is analyzed and the effect of imposing a Kutta condition is discussed from previous works [15,16], in connection with the asymptotic behaviour. Two-dimensional and three-dimensional expressions are compared and applied to the scattering of flap-noise sources by the trailing edge of a wing. The need for including the diffraction effect when predicting the sound radiation from the flap is pointed out. The scattering by a rigid corner is then investigated in Section 3. The exact Green's function is implemented and the asymptotic regime is used to model the high-frequency contribution of flap side-edge noise. In both sections, the specific directivity patterns and the amplification rates associated with the asymptotic regime are quantified.

2. Scattering by a rigid half-plane with flow

After a short survey in Section 2.1 various aspects of edge scattering are addressed.

- The 2D Green's function with flow is presented in Section 2.2. The importance of the Kutta condition is discussed for flow speeds representative of the approach conditions on an aircraft wing or of a subsonic fan blade.
- The 3D Green's function is introduced in Section 2.3. A transposition between the 2D and the 3D fields is also discussed for a far-field observer in the mid-span plane.
- The asymptotic regimes of a source close to the edge and a far-field observer are presented in Section 2.4 where a specific dipole configuration is identified.
- The formalism is applied to a configuration representative of a trailing-edge flap in Section 2.5. The 2D reduction of the theory is also assessed against a 3D formulation. The discussion is made here for dipole sources only, ignoring the Kutta condition.

2.1. State of the art

The scattering of acoustic sources by the edge of an extended flat surface in the presence of flow is a mechanism involved in many aeroacoustic problems. First it is important when assessing the effect of aircraft wings on the sound propagation from engine or propeller-associated sources, and is part of what is called the acoustic installation effect. The primary sources are quadrupoles for jet noise according to Lighthill's acoustic analogy. They are typically equivalent dipoles for rotating blade noise, according to Ffowcs Williams and Hawkings' formulation of the analogy. Dealing with shorter edge-source distances, edge scattering is also expected to play a major role in high-lift device noise, for instance, when the primary sound from the dipole-like sources induced on a deployed flap is diffracted by the main part of the wing. Finally, at even smaller scales, the scattering of boundary-layer turbulence as sound at the trailing-edge of an airfoil is another declination of the same physical process. In this case the sources are equivalent quadrupoles defined by the turbulent mixing and stretching in the boundary layer and the edge-source distance can become much smaller than the acoustic wavelengths. In any case the main flow is responsible for the convection of the acoustic wavefronts radiated from the sources. Furthermore the behaviour of the trailing edge is possibly modified by the formation of a wake.

Many reported works dealing with edge scattering, including the trailing-edge noise theory proposed by Ffowcs Williams and Hall [3], are based on the asymptotic regime for which the observer is in the acoustic far field ($kR \gg 1$) whereas the source point is assumed close to the edge in terms of acoustic wavelengths ($kr_0 \ll 1$). The limit case of a source close to the edge involves a strong amplification and the well-known cardioid directivity pattern, with wavefronts of opposite phases on both sides of the screen [3,17]. Even though this seems justified as a first sight for the quadrupole sources of airfoil trailing-edge noise, no clear evidence of the precise threshold for this regime has been documented yet. The analysis of wing-flap noise reported by Roger and Pérennès [17] and related works [18,19] are also based on the same asymptotic regime for distributed dipoles close to an edge. In this case the approximation is even more questionable, except at the lowest frequencies of interest, because the flap sources are at least several centimeters away from the scattering edge and distributed over the flap chord. The behaviour in the acoustic near-field is also useful for the understanding of the scattering mechanisms; but it cannot be reproduced with the far-field approximation. The asymptotic analyses and the more recent numerical simulations of either trailing-edge noise or sound scattering by an edge finally appear as two opposite approaches, but no or few intermediate investigations are reported, at least to the authors' knowledge.

For all these reasons the present work readdresses edge scattering with arbitrary source and observer locations. It is aimed at quantifying some assumptions often made without precise justification, such as the effect of imposing a Kutta condition, the relevance of a two-dimensional (2D) computation of the acoustic field compared with a more realistic three-dimensional (3D) computation, and the effect of the edge-source distance. The analysis is based on exact half-plane Green's functions for the convected Helmholtz equation.

It is worth noting that, unlike the case of a wedge discussed in Section 3.5, the assumption of uniform fluid motion is here compatible with both a flow parallel to the edge and a flow normal to it in the continuation of the half-plane. The latter configuration corresponds to the classical trailing-edge noise mechanism. The former could be used to investigate the scattering of the boundary-layer turbulence driven in the formation of a tip vortex at the side-edge of a thin flap, at least

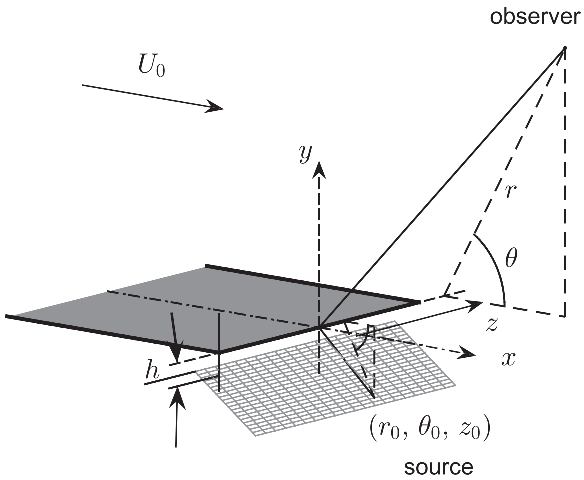

Fig. 2. Reference frame and cylindrical coordinates attached to a half-plane trailing-edge. The surrounding flow of speed U_0 is assumed in the Cartesian x direction. The deployed flap shifted by h downward and considered as equivalent sources distributed on a flat plate is featured in grey.

when the characteristic flow scales remain smaller than the chord but much larger than the actual thickness of the flap (see Section 3.4 and [20]).

The set of cylindrical coordinates for the present derivations is shown in Fig. 2, for intended further application to wing-flap scattering. The flat-plate mimicking the flap is only considered as the location of distributed sources, not as a scattering surface. Cartesian coordinates (x, y, z) are also introduced for convenience with x in the direction of the flow; they will be used for the derivations based on the convected Green's functions. The declination in two dimensions is simply obtained by putting $z = z_0 = 0$.

2.2. Two-dimensional half-plane Green's function

The two-dimensional Green's function for the rigid half-plane in the presence of a uniform mean flow has been derived by Jones [15] and readdressed by Rienstra [16] starting from its expression in a quiescent medium first proposed by MacDonald [14]. The formulation includes an optional correction accounting for a full Kutta condition at the trailing edge. For a trace of the half-plane at $y = 0$ and $x < 0$ in Cartesian coordinates (see Fig. 2) and for a uniform flow of Mach number M_0 in the positive x direction, the expression reads

$$G_{M_0}(\mathbf{x}, \mathbf{x}_0, k) = \frac{1}{\beta}\, \mathrm{e}^{-\mathrm{i}KM_0(X - X_0)} \left[G^{(1/2)}_{M_0}(\mathbf{x}, \mathbf{x}_0, k) + G_K(\mathbf{x}, \mathbf{x}_0, k) \right],$$

where $\mathbf{x} = (x, y)$ and $\mathbf{x}_0 = (x_0, y_0)$ are the observer and source vectors respectively. The dependence $\mathrm{e}^{-\mathrm{i}\omega t}$ of monochromatic waves is implicitly assumed. The first term in the square brackets $G^{(1/2)}_{M_0}$ is the classical half-plane Green's function corrected for the convection by the flow, written as

$$4\pi G^{(1/2)}_{M_0}(\mathbf{x}, \mathbf{x}_0, k) = \int_{-\infty}^{s_1} \mathrm{e}^{\mathrm{i}K\overline{r}_1\sqrt{1+u^2}} \frac{\mathrm{d}u}{\sqrt{1+u^2}} + \int_{-\infty}^{s_2} \mathrm{e}^{\mathrm{i}K\overline{r}_2\sqrt{1+u^2}} \frac{\mathrm{d}u}{\sqrt{1+u^2}}. \tag{1}$$

In Eq. (1) $\overline{r}^2_{1,2} = \overline{r}^2 + \overline{r}^2_0 - 2\overline{r}\,\overline{r}_0 \cos\,(\overline{\theta} \mp \overline{\theta}_0)$, the subscript 0 referring to the source location. $K = k/\beta$, $\beta = \sqrt{1 - M_0^2}$; $\overline{r} = \sqrt{X^2 + y^2}$ is the corrected observer distance to the edge with $X = x/\beta$ and

$$s_1 = \frac{2\sqrt{\overline{r}_0\overline{r}}}{\overline{r}_1} \cos \frac{\overline{\theta} - \overline{\theta}_0}{2}, \quad s_2 = -\frac{2\sqrt{\overline{r}_0\overline{r}}}{\overline{r}_2} \cos \frac{\overline{\theta} + \overline{\theta}_0}{2}.$$

The angles $\overline{\theta}$ and $\overline{\theta}_0$ are defined as the corrected angles from the wake direction $x > 0$ such that

$$\cos\,\overline{\theta} = \frac{X}{\sqrt{X^2 + y^2}}, \quad \cos\,\overline{\theta}_0 = \frac{X_0}{\sqrt{X_0^2 + y_0^2}}.$$

The second term is the correction needed to account for the Kutta condition at the edge. It reads

$$4\pi G_K(\mathbf{x}, \mathbf{x}_0, k) = \frac{A_0}{2} \frac{\mathrm{e}^{-\mathrm{i}\pi/4}}{\sqrt{\pi}}\, \mathrm{e}^{\mathrm{i}K\overline{r}} \left[F^*\left(\sqrt{2K\overline{r}}\, \sin \frac{\overline{\theta} - \overline{\theta}_1}{2} \right) + F^*\left(\sqrt{2K\overline{r}}\, \sin \frac{\overline{\theta} + \overline{\theta}_1}{2} \right) \right] - \frac{A_0}{2} 2\, \mathrm{e}^{\mathrm{i}KX/M_0} \cosh\left(\frac{\beta K}{M_0} y \right) H(-y), \tag{2}$$

where the factor A_0 is given by Jones as

$$\frac{A_0}{2} = \text{sign}(y_0)\sqrt{\frac{2\pi}{K\overline{r}_0}}\sqrt{1-\frac{X_0}{\overline{r}_0}}\sqrt{\frac{M_0}{1+M_0}}\,\mathrm{e}^{\mathrm{i}K\overline{r}_0+\mathrm{i}\pi/4}$$

and where $\overline{\theta}_1$ is an imaginary angle such that $\cos\overline{\theta}_1 = 1/M_0$. H is the Heaviside function and F is the complex function of complex argument defined by

$$F(z) = \mathrm{e}^{\mathrm{i}z^2}\int_z^{\infty}\mathrm{e}^{-\mathrm{i}t^2}\,\mathrm{d}t = \frac{\sqrt{\pi}}{2}\mathrm{e}^{-\mathrm{i}\pi/4}\,\mathrm{e}^{\mathrm{i}z^2}\,\mathrm{erfc}\left(\mathrm{e}^{\mathrm{i}\pi/4}\,z\right)$$

and better expressed in terms of the complementary error function for computations [21]. Eq. (2) is referred to as the Kutta correction later on. It must be noted that Eqs. (1) and (2) include the additional factor 4π with respect to the original expressions in [15,16] because Green's function is defined as the response to a unit impulse in the Helmholtz equation.

In the present context of aerodynamic noise sources, the sound field is needed only for dipoles and/or quadrupoles, depending on the resorted formulation of the analogy. The acoustic pressure of a point dipole of strength $\mathbf{F}$ is related to the gradient of Green's function with respect to the source coordinates, as $p(\omega, r) = \nabla G(\mathbf{x}, \mathbf{x}_0)\cdot\mathbf{F}(\omega)$. When applied to Eq. (1), this involves the numerical evaluation of integrals of the types

$$\int_{-\infty}^{s_1}\mathrm{e}^{\mathrm{i}K\overline{r}_1\sqrt{1+u^2}}\frac{\mathrm{d}u}{\sqrt{1+u^2}}\quad\text{and}\quad\int_{-\infty}^{s_1}\mathrm{e}^{\mathrm{i}K\overline{r}_1\sqrt{1+u^2}}\,\mathrm{d}u.$$

Unlike the integrals of the first type, the integrals of the second type have no definite value, except if the wavenumber K is given a small negative imaginary part. This artificial damping is assumed here implicitly and the limit of the result as the imaginary part goes to zero is taken at the end of the derivations. For both integrals the integration range is split into two ranges from $-\infty$ to 0 and from 0 to s_1. Eventually performing the change of variable $u' = \sqrt{1+u^2}$ in the negative range of u yields the results [22]

$$\begin{aligned}\int_{-\infty}^{s_1}\mathrm{e}^{\mathrm{i}K\overline{r}_1\sqrt{1+u^2}}\frac{\mathrm{d}u}{\sqrt{1+u^2}} &= \int_0^{s_1}\mathrm{e}^{\mathrm{i}K\overline{r}_1\sqrt{1+u^2}}\frac{\mathrm{d}u}{\sqrt{1+u^2}} + K_0^*(\mathrm{i}K\overline{r}_1),\\ \int_{-\infty}^{s_1}\mathrm{e}^{\mathrm{i}K\overline{r}_1\sqrt{1+u^2}}\,\mathrm{d}u &= \int_0^{s_1}\mathrm{e}^{\mathrm{i}K\overline{r}_1\sqrt{1+u^2}}\,\mathrm{d}u + K_1^*(\mathrm{i}K\overline{r}_1),\end{aligned}\tag{3}$$

where K_n^* stands for the complex conjugate of the modified Bessel function, related to the Hankel function as

$$\mathrm{K}_n^*(\mathrm{i}x) = \frac{\mathrm{i}\pi}{2}\,\mathrm{e}^{\mathrm{i}n\pi/2}H_n^{(1)}(x).$$

The remaining parts of the integrals are computed by numerical quadrature over the constant interval $[0, 1]$ using the change of variable $u = s_1 t$.

In the same way the field of a point quadrupole is given by the double scalar product of the quadrupole strength tensor $\mathbf{Q}$ and of the second gradient of Green's function with respect to the source coordinates, say $p(\omega, r) = \mathbf{Q}(\omega)\cdot\cdot\nabla\nabla G(\mathbf{x}, \mathbf{x}_0)$. This leads to an integral with a diverging oscillatory integrand. But performing an integration by parts in this integral yields

$$\int_{-\infty}^{s_1}\sqrt{1+u^2}\,\mathrm{e}^{\mathrm{i}K\overline{r}_1\sqrt{1+u^2}}\,\mathrm{d}u = \int_0^{s_1}\sqrt{1+u^2}\mathrm{e}^{\mathrm{i}K\overline{r}_1\sqrt{1+u^2}}\,\mathrm{d}u + K_2^*(\mathrm{i}K\overline{r}_1) - \frac{K_1^*(\mathrm{i}K\overline{r}_1)}{\mathrm{i}K\overline{r}_1}.$$

This splitting has been used for the implementation. Though the derivatives generate cumbersome expressions they can be implemented in a straightforward way to predict the radiated field of arbitrary source distributions by linear superposition. This ensures the maximum accuracy by avoiding a numerical treatment of the derivatives, on the one hand, and makes the analytical solutions a reference for the validation of numerical techniques developed elsewhere, on the other hand. Furthermore exact Green's functions give accurate access to the sound field in the shadow zones of obstacles, unlike simplified approaches. The shadow zones are defined as the areas from where the source cannot be seen.

Sample results for point dipoles in the vicinity of a trailing edge are reported in Fig. 3. The Mach number is 0.29 and the dipole inclination angle is $\alpha_d = \pm 50^\circ$ as measured from the flow direction. The Kutta correction is taken into account. It is responsible for a concentrated contribution along the wake in the continuation of the half-plane. The downstream expansion of the corresponding trace is only an artefact of the plotting program on a polar mesh. It exhibits the space periodicity of a pure convected pattern, with an aerodynamic wavelength smaller than the acoustic wavelength. In all plots the characteristic wavefronts of the free-field dipole remain recognizable, with distortions induced by the diffraction. The dashed lines indicate the boundaries of the shadow zones. When the main lobe of the dipole impinges on the edge significant sound is regenerated in the shadow zone of the half-plane (cases with $\theta_0 = 45^\circ$, $\alpha_d = 50^\circ$). In contrast as the dipole source is located well away from the edge such as in the case of the upper right plot ($\alpha_d = 50^\circ, \theta_0 = 135^\circ$), the half-plane behaves like a reflecting screen: interference patterns are seen in the upper half-space and sound extinction is very effective in the lower half-space. For the parametric tests reported in Fig. 3 it has been verified that Jones' solution for the Kutta correction does not affect significantly the acoustic wavefront structure away from the wake. As the dipole approaches the edge at distances much shorter than the wavelength, the radiated field progressively experiences a fundamental change of the wavefront structure. This is illustrated in Fig. 4 for the dipole inclined by $\alpha_d = 50^\circ$ and at the source angle $\theta_0 = 45^\circ$.

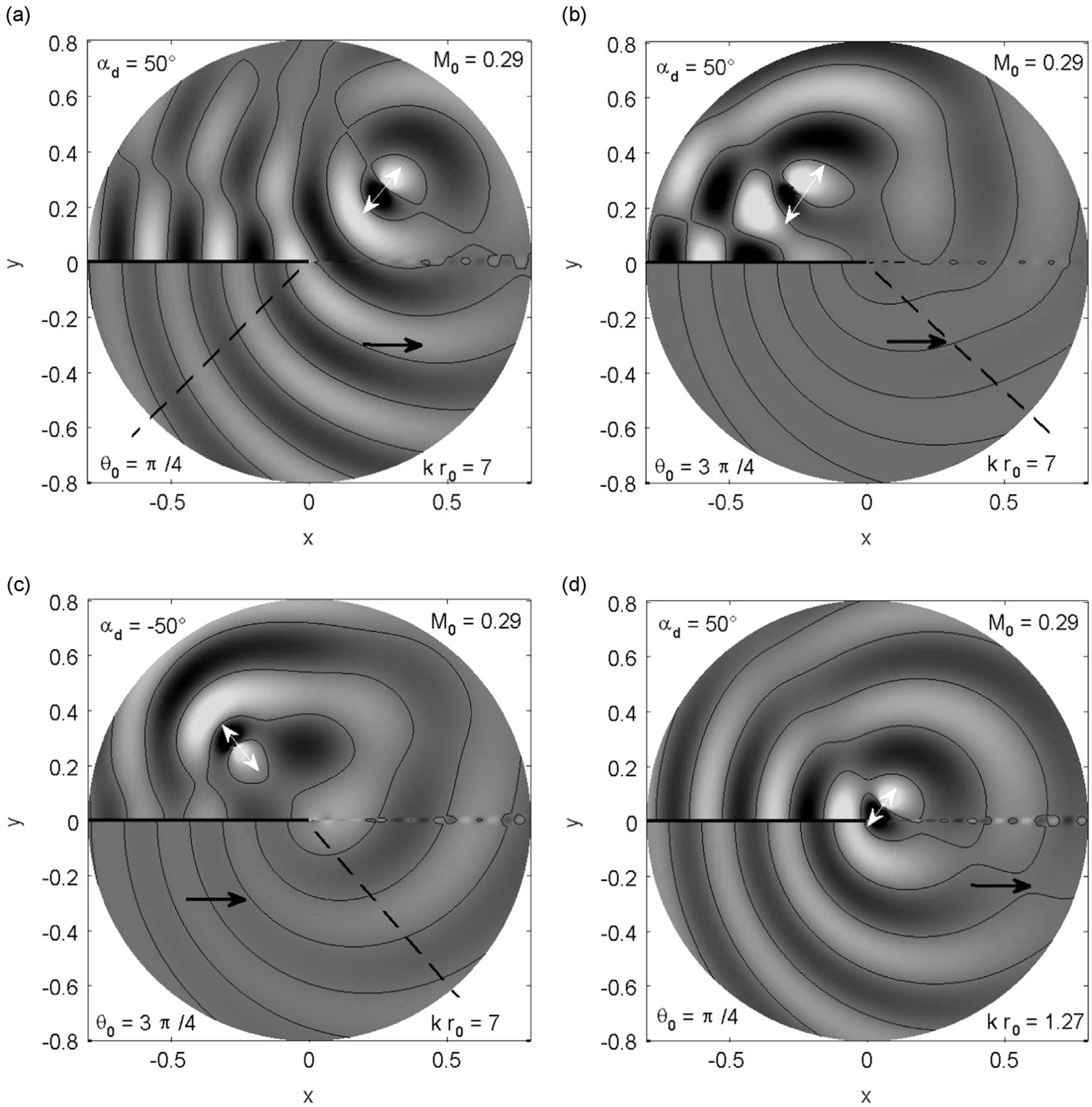

Fig. 3. Instantaneous wavefronts of point dipoles close to a scattering edge in the presence of uniform flow. Mach number 0.29, flow from left to right. Half-plane featured by the thick horizontal line. Kutta correction included. Bounds of the shadow areas indicated by dashed lines.

Wavefronts of opposite phases tend to form on both sides of the half-plane. Furthermore the radiation is enhanced upstream and goes to zero downstream in the wake. This corresponds to the cardioid far-field sound directivity diagram classically reported according to the basic factor $\sin(\theta/2)$ relevant at vanishing Mach numbers (see Section 2.4 and for instance [23]). At the same time the sound radiation is amplified as the asymptotic regime is entered. Indeed the amplitude was divided by 3 for the plot in Fig. 4b in order to compare the wavefront structures of Fig. 4a and b.

Typical wavefront patterns of a mixed quadrupole in the vicinity of the edge of a half-plane are shown in Fig. 5. The quadrupole strength is defined by the components $T_{11} = (1+\mathrm{i})^2/4$, $T_{22} = (1-\mathrm{i})^2/4$ and $T_{12} = -2(1+\mathrm{i})(1-\mathrm{i})/4$. This source produces a characteristic wavefront pattern with four spiral branches in free field. It is representative of the leapfrogging of vortices as described by Bogey et al. [24]. Angles $\theta_0 = \pm 45^\circ$ and $\theta_0 = 135^\circ$, and two source-edge distances $kr_0 = 1.57$ and $kr_0 = 0.157$ are selected. For the largest distance the amplitude of the sound field is close to what would be found without scattering. For $\theta_0 = -45^\circ$ the resulting sound field appears as very similar to the free-field spiral-like pattern. Two dark branches and two light ones can be identified. One of them is indicated by the white arrows in Fig. 5a. The pattern rotates in the counterclockwise direction. This result means that the scattering is ineffective, essentially because the incident acoustic wavefronts propagate upstream normal to the half-plane. In contrast a clear shadow zone is found below the half-plane for $\theta_0 = 135^\circ$ because the primary sound from the quadrupole is reflected upstream. It gives rise to a slight reinforcement above the half-plane instead of interference patterns because the distance from the source to its image remains smaller than the

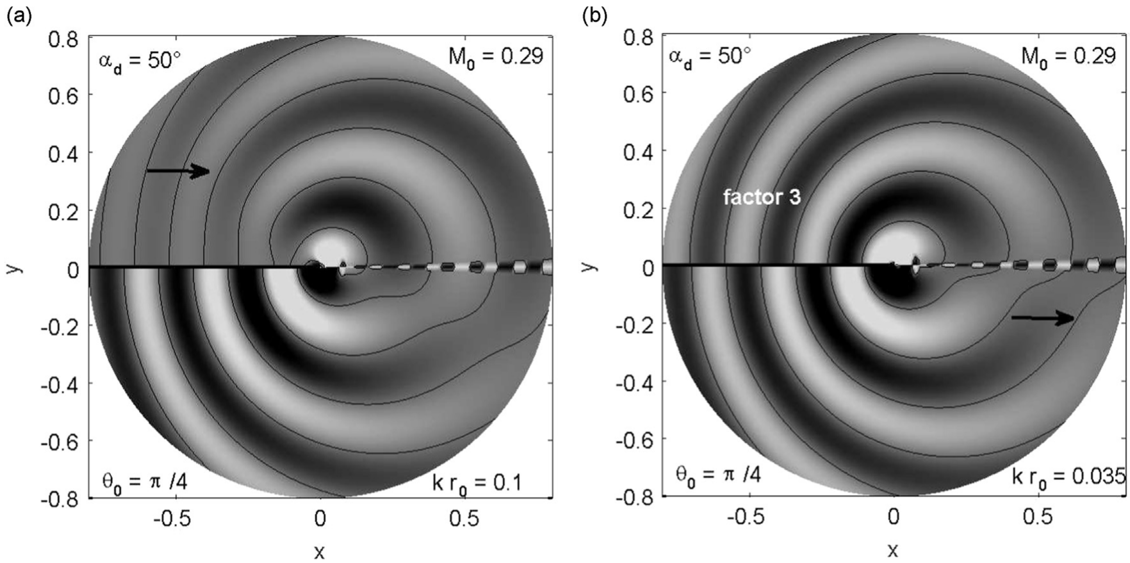

Fig. 4. Asymptotic sound field for a dipole approaching the edge in the presence of uniform flow. Mach number 0.29, flow from left to right. Half-plane featured by the thick horizontal line. Kutta correction included. Same grey scale as in Fig. 3, attenuated by a factor 3 in plot (b).

wavelength. For a ten times smaller source-to-edge distance the pressure field again exhibits the characteristic cardioid pattern of the asymptotic regime, irrespective of the source angle θ_0. The quadrupole behaviour of the source is lost at the benefit of the phase opposition between both sides of the plate. Furthermore the amplitude scale has been divided by the factor 5 before plotting, which again means that the radiation is also much stronger. No Kutta condition is applied in this test in order to focus on the effect of reducing the parameter kr_0 on the integrals involved in Green's function.

Now the asymptotic range ($kr_0 \ll 1$) precisely involves the maximum effect of the Kutta condition. This is emphasized by the numerical test made with the exact 2D solution and reported in Fig. 6 for the aforementioned point quadrupole at the two flow Mach numbers of 0.06 and 0.35. These values would typically correspond to a low-speed fan blade and to the maximum speed over an aircraft wing at approach, respectively. The ratio Δ of the amplitudes of solutions with and without Kutta correction is plotted as a function of the dimensionless distance kr_0 in equivalent decibels. This makes sense because both directivity diagrams exhibit the same cardioid pattern in this limit behaviour. Δ roughly increases from 1 dB to 12 dB as kr_0 drops from 0.26 to 0.026 at the lowest speed, and from 5 dB to 23 dB at the highest speed. The expected value for larger kr_0 is about 0 at $M_0 = 0.06$, suggesting that the Kutta condition has no effect. Though these indicative results are far from complete, it can be concluded that the amplification by the Kutta condition generally increases with increasing Mach number and decreasing source-to-edge distance in terms of wavelengths. At vanishingly small values of kr_0, the amplitude ratio in decibels goes proportional to the inverse distance.

In all applications for which trailing-edge noise is a significant contribution, the amplification by the Kutta condition as formulated by Jones appears a crucial mechanism. As an example for a boundary-layer thickness of 4 mm and a frequency of 2 kHz typical of low-speed fan noise in air-cooling technology, kr_0 roughly ranges from 0 to 0.15. The upper bound corresponds to eddies well removed from the edge, for which the asymptotic behaviour is not likely to take place. In contrast much smaller values enter the asymptotic regime of amplification. At the same time the amplitude of the velocity fluctuations, thus the strength of the quadrupole sources is expected to drop to zero at the wall due to viscosity. As a consequence, a practical lower bound for the parameter kr_0 is expected from physical considerations, and the over-amplification by the Kutta correction is probably limited.

2.3. Three-dimensional half-plane Green's function

The results of Section 2.2 and other tests not reproduced in this study suggest that, as long as a dipole or a quadrupole is not very close to the edge, the effect of the Kutta correction can be ignored for subsonic flows of Mach numbers up to 0.3. In such cases the 2D Green's function accounting for the presence of a uniform flow is simply obtained from the corresponding Green's function in a quiescent fluid by stretching the streamwise coordinate according to $X = x/\beta$ and by multiplying by the factor $\mathrm{e}^{-\mathrm{i}KM_0(X-X_0)}$. The same transform holds in a three-dimensional space for a fluid motion normal to the spanwise direction. Therefore, edge scattering in 3D can be simply assessed from a direct extension of the expression given by MacDonald [14] for a medium at rest. Green's function for the convected Helmholtz equation now reads

$$G^{(3D)}_{M_0}(\mathbf{x},\mathbf{x}_0) = \frac{-\mathrm{i}K}{4\pi^2\beta}\,\mathrm{e}^{-\mathrm{i}KM_0(X-X_0)} \times \left\{ \int_{-\infty}^{S_1} \frac{K_1^*(\mathrm{i}K\overline{r}_1\sqrt{1+u^2})}{\sqrt{1+u^2}}\,\mathrm{d}u + \int_{-\infty}^{S_2} \frac{K_1^*(\mathrm{i}K\overline{r}_2\sqrt{1+u^2})}{\sqrt{1+u^2}}\,\mathrm{d}u \right\}, \tag{4}$$

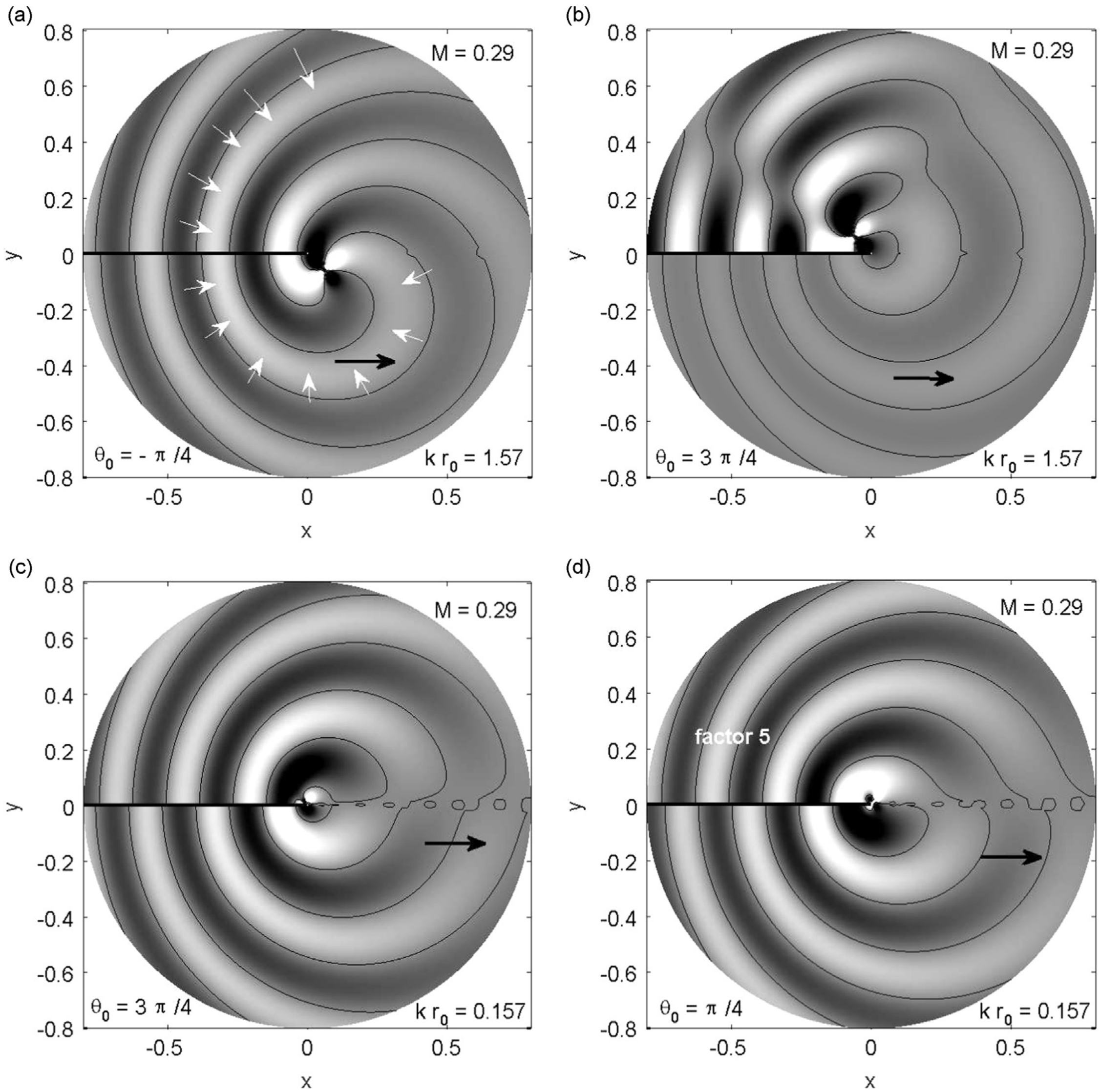

Fig. 5. Instantaneous wavefronts of point leap-frogging quadrupoles close to a scattering edge in the presence of uniform flow. Mach number 0.29, flow from left to right. Half-plane featured by the thick horizontal line. Evidence of the asymptotic cardioid regime for $kr_0 = 0.157$; grey scale attenuated by a factor 5 in plots (c) and (d). No Kutta correction.

where the notations $(\overline{r}_j, S_j)$ are similar to $(\overline{r}_j, s_j)$ of Section 2.2, except that the spanwise quantity $(z-z_0)^2$ is added to the definition of $\overline{r}_i^2$, z and z_0 denoting the spanwise locations of the observer and of the source, respectively. Provided that the observer lies in the mid-span plane assuming $z = z_0$ and that the source terms have no component in the spanwise direction, the derivations of the acoustic field for dipoles or quadrupoles are similar to the ones made in previous sections. This is more obvious for high-lift device noise sources if they are precisely interpreted as dipoles normal to the flap surface. Thus comparing the radiated dipole fields according to both the 3D-midspan and 2D models makes sense. In contrast, quadrupoles could justify imposing a Kutta condition since they are possibly distributed very close to the edge of the wing. Deriving a 3D Kutta correction which would extend Jones' analysis has not been attempted here. This could be the matter for a future work.

It is worth noting that the 3D and 2D half-plane Green's functions are related to each other. The cylindrical wave field of the 2D function is exactly reproduced from the 3D function by continuously distributing the same point source from $z_0 = -\infty$ to $z_0 = +\infty$ and integrating between these two limits. Indeed it is found that

$$\frac{-\mathrm{i}K}{\pi} \int_{-\infty}^{\infty} \int_{-\infty}^{S_j} \frac{K_1^*(\mathrm{i}K\overline{r}_j\sqrt{1+u^2})}{\sqrt{1+u^2}} \,\mathrm{d}u \,\mathrm{d}\eta = \int_{-\infty}^{s_j} \frac{\mathrm{e}^{\mathrm{i}K\overline{r}_j\sqrt{1+u^2}}}{\sqrt{1+u^2}} \,\mathrm{d}u,$$

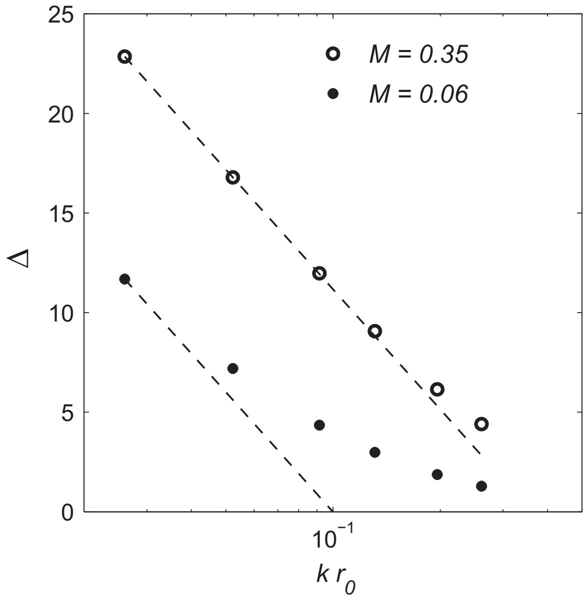

Fig. 6. Kutta-condition amplification on a lateral quadrupole in the limit of small kr_0. Δ: amplitude ratio of the solutions with and without Kutta correction in dB. (- - -): $(kr_0)^{-1}$ asymptotic trend.

with $\eta = z - z_0$, by first introducing the following identities:

$$K_1^*(\mathrm{i}\xi) = \frac{1}{2}\int_{-\infty}^{\infty} \mathrm{e}^{\mathrm{i}\xi\sqrt{1+t^2}}\,\mathrm{d}t, \quad K_0^*(\mathrm{i}\xi) = \frac{1}{2}\int_{-\infty}^{\infty} \frac{\mathrm{e}^{\mathrm{i}\xi\sqrt{1+t^2}}}{\sqrt{1+t^2}}\,\mathrm{d}t$$

and next permuting the integrations with respect to the variables t and η.

The first application of the present formalism is the derivation of the field of a point dipole, as the theoretical background for addressing High-Lift Device noise. In forming the scalar product of the dipole source strength and the first gradient of Green's function, the following integrals are found:

$$\int_0^{\infty} \frac{K_1^*(\mathrm{i}K\overline{r}_j\sqrt{1+u^2})}{\sqrt{1+u^2}}\,\mathrm{d}u = \int_0^{\infty} K_0^*\left(\mathrm{i}K\overline{r}_j\sqrt{1+u^2}\right)\,\mathrm{d}u = \mathrm{i}\,\frac{\pi}{2}\,\frac{\mathrm{e}^{\mathrm{i}K\overline{r}_j}}{K\overline{r}_j} \tag{5}$$

and the complementary parts between 0 and S_i are computed numerically using the same method as in Section 2.2.

The special case of an observer both in the acoustic far field and in the mid-span plane of the wing of an aircraft is a configuration of primary interest. It corresponds to $(\overline{r}_j, S_j) = (\overline{r}_j, s_j)$ if the wing is modelled by a rigid scattering half-plane. In this case a possible approach for simulating the sound field in 3D from a 2D computational procedure is known as Oberai's transposition formula [25], applied to long-span bodies by other authors [26]. This transposition relates the distant 3D field to the 2D field evaluated with the same source. It is based on a splitting of the 3D field into cylindrical harmonics and on the theorem of stationary phase. The extension of the formula initially derived for a stationary propagation medium to the case of a uniformly moving one is straightforward and reads

$$\phi^{3D} \simeq \phi^{2D}\,\mathrm{e}^{-\mathrm{i}\pi/4}\sqrt{\frac{K}{2\pi\overline{r}}}, \tag{6}$$

where ϕ^{3D} and ϕ^{2D} stand for the acoustic potentials, with the present notations. Its practical use in connection with HLD noise is relevant for an observer in the distant field and in the mid-span plane of an aircraft wing segment. Because the underlying asymptotic development is not very accurate, the validity of the transposition formula needs to be assessed; this is achieved in Section 2.5, for dipole sources only.

The application to the scattering of quadrupoles requires deriving the second gradient of Green's function, which leads to cumbersome developments and additional integrals that must be reduced using the same principle as for Eq. (5). Details of the implementation are given in the Appendix. Sample results are shown in Fig. 7 for the same leapfrogging quadrupole as in Section 2.2, other source coefficients T_{ij} being zero. The sound field is analyzed in the plane normal to the edge and containing the source. The mean-flow Mach number is 0.29. Two configurations involving different locations with respect to the edge are considered. For the dimensionless distance $kr_0 = 5$ the spiral wavefronts are still recognized in the upper part of the plot. Because the quadrupole is located above the half-plane a significant reflection occurs in this region, where the interfering wavefronts feature a travelling wave along the upper surface. The shadow region receives a low-level contamination from the trailing-edge scattering. The diffraction is much more critical in the case of a lower dimensionless

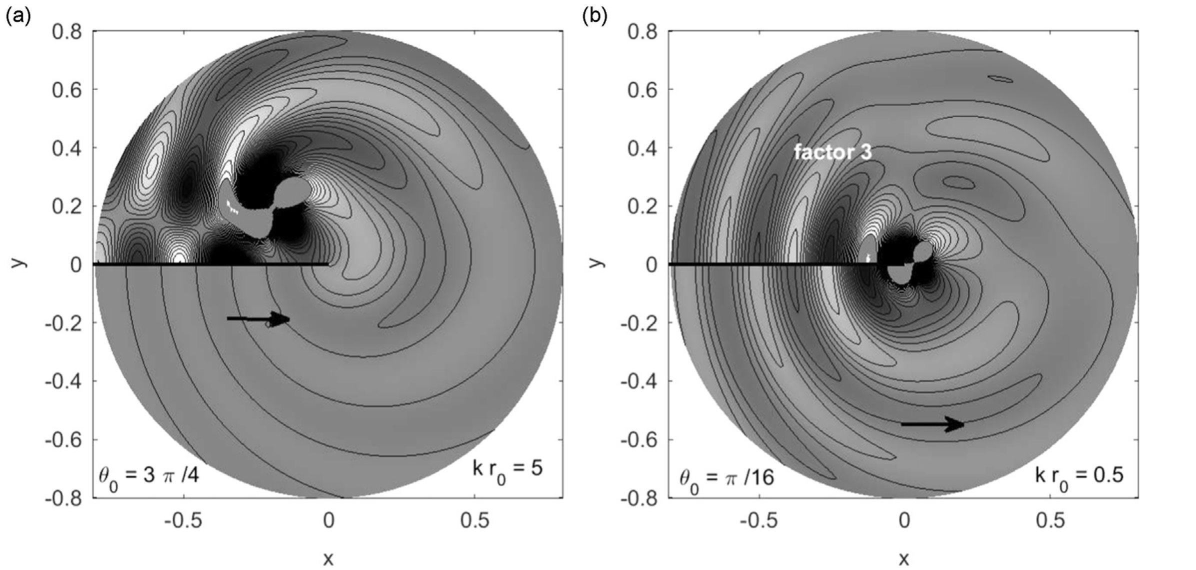

Fig. 7. Typical instantaneous wavefront patterns for a leapfrogging quadrupole close to the edge of a half-plane, according to the three-dimensional Green's function. Mach number 0.29, flow from left to right. (a) Distant source. (b) Source close to the edge.

distance $kr_0 = 0.5$. The configuration approaches the asymptotic regime for which a cardioid pattern is again observed, except for the relative extinction angle in the upper half-space. Negligible sound is heard in the wake and out-of-phase waves travel upstream on both sides of the half-plane. The results confirm the behaviours observed with the two-dimensional Green's function. They are believed to be representative of some of the installation effects on jet noise. The sound from the primary sources of a turbofan engine jet under the wing of an aircraft is scattered by the edge of the wing. If the source-to-wing distance is larger than the acoustic wavelengths the effect reduces to ordinary reflection and diffraction at the edge with no crucial change in the efficiency and the fundamental radiating properties of the source (Fig. 7a). The effect could be approximately reproduced with geometrical arguments. In contrast if the sources are very close to the edge their quadrupole nature is completely restructured by the scattering (Fig. 7b). This rather corresponds to a jet which interacts aerodynamically with part of the wing or with a trailing-edge flap. In this case the wing strongly modifies the development of the jet in practice. Furthermore it becomes questionable to independently consider fluctuations coming from the jet mixing and from boundary-layer turbulence. Mathematically both contributions are described in the same way except that characteristic scales such as turbulent eddy sizes are larger for the jet in the downstream fully developed region than for the boundary-layer flow.

2.4. Asymptotic analysis and zero-amplification dipole configuration

The asymptotic cardioid radiation pattern and the associated amplification are observed as a point dipole gets closer and closer to the edge in terms of acoustic wavelengths. Yet, this general behaviour admits exceptions for special combined values of the dipole angle α_d and of its angular location θ_0. The exceptions correspond to a total cancellation of the contribution coming from the definite integrals involved in Green's function. This aspect is independent of the Kutta condition and is the only remaining one if A_0 is set to zero in Eq. (2). Evidence of such a deviation from the asymptotic cardioid regime is shown in Fig. 8 where the solutions with and without Kutta correction are compared for $kr_0 = 0.0924$ with $\alpha_d = \pi/4$ and $\theta_0 = \pi/2$. The Kutta-corrected solution exhibits the high-amplitude cardioid pattern with opposite phases on both sides of the half-plane (the grey scale is divided by a factor 3 for the comparison). In contrast the no-Kutta solution turns to another dipole-like pattern aligned with the direction $\theta = 0$, free of any amplification; therefore imposing the Kutta condition or not produces dramatically different solutions. The origin of this special behaviour is explained now based on an asymptotic analysis, from which the Kutta correction is discarded.

The asymptotic expressions of the 2D and 3D Green's functions are derived from the exact ones by simple developments, briefly outlined here. First the modified Bessel functions are expanded for large arguments as

$$K_{0,1}(\mathrm{i}\xi) \sim \sqrt{\frac{\pi}{2\mathrm{i}\xi}}\,\mathrm{e}^{-\mathrm{i}\xi}$$

and the bounds of the definite integrals are approximated as

$$s_{1,2} \simeq \pm 2\sqrt{\frac{\overline{r}_0}{\overline{r}}}\,\cos\left(\frac{\overline{\theta} \mp \overline{\theta}_0}{2}\right),$$

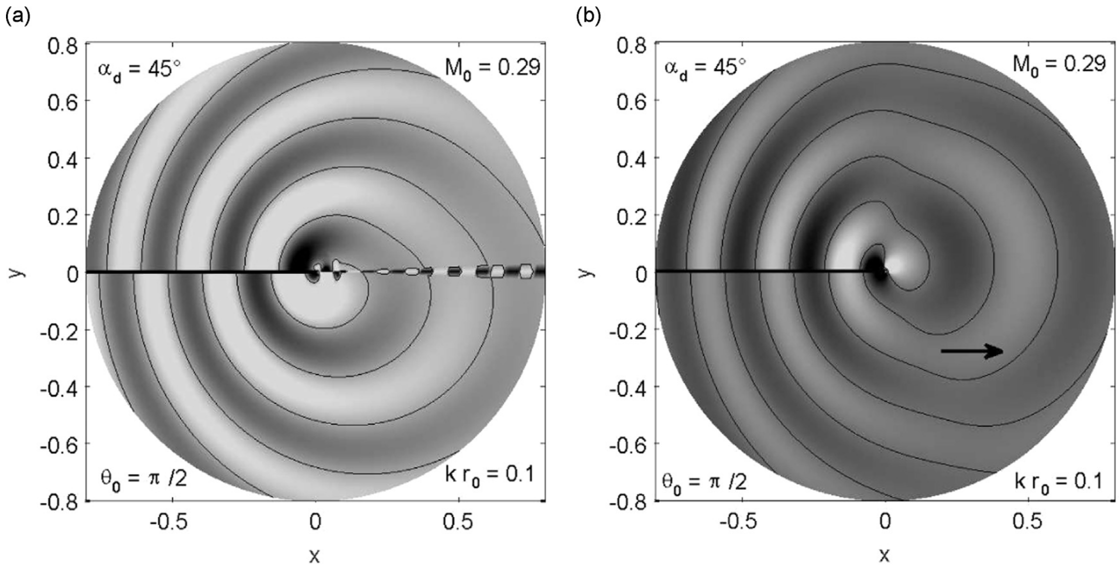

Fig. 8. Wavefront patterns for an oblique dipole very close to the edge, according to the solutions with (a) and without (b) Kutta correction; critical configuration $\alpha_d = (\pi - \theta_0)/2$. Grey scale of plot (a) attenuated by a factor 3. Parameters indicated on the plot.

provided that $(z - z_0)$ remains small. Equivalently the observer is assumed not approaching the plane $z=0$. As a result the integrals are approximated as

$$\frac{-\mathrm{i}K}{\pi}\int_{-\infty}^{S_1}\frac{K_1^*(\mathrm{i}K\overline{r}_1\sqrt{1+u^2})}{\sqrt{1+u^2}}\,\mathrm{d}u \sim \frac{\mathrm{e}^{\mathrm{i}K\overline{r}}}{2\overline{r}} - \frac{\mathrm{i}K}{\pi}\sqrt{\frac{\mathrm{i}\pi}{2K\overline{r}}}\int_0^{S_1}\frac{\mathrm{e}^{\mathrm{i}K\overline{r}\sqrt{1+u^2}}}{(1+u^2)^{3/4}}\,\mathrm{d}u$$

and

$$\int_{-\infty}^{s_1}\frac{\mathrm{e}^{\mathrm{i}K\overline{r}_1\sqrt{1+u^2}}}{\sqrt{1+u^2}}\,\mathrm{d}u \sim \mathrm{e}^{\mathrm{i}(K\overline{r}+\pi/4)}\sqrt{\frac{\pi}{2K\overline{r}}} + \int_0^{s_1}\frac{\mathrm{e}^{\mathrm{i}K\overline{r}\sqrt{1+u^2}}}{\sqrt{1+u^2}}\,\mathrm{d}u$$

for the 3D and 2D cases, respectively, and similar expressions with S_2 and s_2. $S_{1,2}$ and $s_{1,2}$ are small quantities in the limit of sources very close to the edge, therefore the integrals can be assimilated to their upper bounds. This leads to the asymptotic forms of the 3D and 2D Green's functions as

$$G_{M_0}(\mathbf{x},\mathbf{x}_0) \sim \frac{\mathrm{e}^{\mathrm{i}K(\overline{r}-M_0X)}}{4\pi\beta\overline{r}}\left\{1 + 2\frac{\mathrm{e}^{-\mathrm{i}\pi/4}}{\sqrt{\pi}}(2K\overline{r}_0\,\sin\,\varphi)^{1/2}\,\sin\,\frac{\overline{\theta}_0}{2}\,\sin\,\frac{\overline{\theta}}{2}\right\}, \quad (7)$$

$$G_{M_0}(\mathbf{x},\mathbf{x}_0) \sim \sqrt{2\pi}\,\frac{\mathrm{e}^{\mathrm{i}(K(\overline{r}-M_0X)+\pi/4)}}{4\pi\sqrt{\beta K\overline{r}}}\left\{1 + 2\frac{\mathrm{e}^{-\mathrm{i}\pi/4}}{\sqrt{\pi}}(2K\overline{r}_0)^{1/2}\,\sin\,\frac{\overline{\theta}_0}{2}\,\sin\,\frac{\overline{\theta}}{2}\right\}, \quad (8)$$

respectively. φ denotes the angle of the projection of the observer in the plane (y,z) with respect to the y axis.

The 2D asymptotic Green's function in free field would be obtained from the limit of the Hankel functions for large arguments as

$$G_\infty(\mathbf{x},\mathbf{x}_0) \sim \frac{\mathrm{e}^{\mathrm{i}\pi/4}}{4\beta}\sqrt{\frac{2}{\pi K\overline{r}}}\mathrm{e}^{\mathrm{i}K(\overline{r}-M_0X)}.$$

Therefore the factors in front of the curly brackets in Eqs. (7) and (8) coincide with the far-field approximations in free field.

The same expression is found in the brackets as soon as $\varphi = \pi/2$, which stresses the fact that the scattering is fundamentally a cylindrical process even in a three-dimensional space. Furthermore the ratio of both functions is identical to Oberai's transposition formula (Eq. (6)). Because source-associated space derivatives of Green's function are involved in the radiation by multi-pole sources, the term 1 in the brackets has no effect and factors $(K\overline{r}_0)^{-1/2}$ and $(K\overline{r}_0)^{-1}$ are produced, for dipoles and quadrupoles respectively. Since $K\overline{r}_0$ is a small parameter, the net result is some amplification of the natural radiation by the sources. Furthermore the asymptotic directivity is determined by the factor $\sin(\overline{\theta}/2)$ and features a cardioid pattern in the limit of low Mach numbers, no sound being radiated in the continuation of the half-plane and the maximum sound being radiated along the half-plane. These asymptotic results are confirmed by the exact simulations in (Figs. (4) and 5). Though the derivations are not detailed here, the 3D sound field of a dipole of strength P and of angle α_d is easily obtained from the asymptotic formulation, Eq. (7), as

$$p(\mathbf{x},\omega)=\frac{\mathrm{e}^{\mathrm{i}K(\overline{r}-M_0X)}}{4\pi\beta\overline{r}}\frac{\mathrm{e}^{-\mathrm{i}\pi/4}}{\sqrt{\pi}}\sin\frac{\overline{\theta}}{2}\frac{2K\sqrt{\sin\varphi}}{\sqrt{2K\overline{r}}}\left\{-\sin\frac{\overline{\theta}_0}{2}\sin\alpha_d+\beta\cos\frac{\overline{\theta}_0}{2}\cos\alpha_d\right\}P,$$

or in the limit of vanishing Mach numbers for which $\overline{\theta}=\theta$ and $\overline{\theta}_0=\theta_0$

$$p_0(\mathbf{x},\omega)=\frac{\mathrm{e}^{\mathrm{i}kR}}{4\pi R}\frac{k\,\mathrm{e}^{-\mathrm{i}\pi/4}}{(2\pi)^{3/2}}\sin\frac{\theta}{2}\left(\frac{\sin\varphi}{kr_0}\right)^{1/2}\cos\left(\alpha_d+\frac{\theta_0}{2}\right)P.$$

As a result the acoustic pressure drops to zero if $\alpha_d+\theta_0/2=\pi/2$ in a quiescent fluid or close to that condition in a subsonic flow. This means that the dominant term according to the asymptotic analysis is exactly zero. Sound is still produced by all terms neglected in the developments, at a much lower level of the same order of magnitude as the free-field radiation. The cancellation of the dominant term is not believed to occur in real HLD systems because the flap is positioned below the wing trailing edge. Therefore amplification is always expected at the lowest frequencies.

2.5. Distributed flap-noise sources

The edge-scattering model of Section 2.3 is now used jointly with a source model of the lift induced on an airfoil by incident turbulence in order to illustrate the scattering of flap noise by the wing of an aircraft. Complementary trailing-edge noise sources that take place at both trailing edges of the wing and of the flap are discarded from the analysis. The interest is focussed on the amount of scattering and the subsequent free-field and installed radiation features for distributed sources that concentrate at the leading edge of the flap.

The induced unsteady lift on the flap acting as sources at a given frequency is modeled using Amiet's theory [27]. A single parallel gust (Fourier component) is considered, for which the unsteady lift distributes as

$$\ell(y_1^*)=\frac{2\rho_0U_0\tilde{w}\mathrm{e}^{\mathrm{i}\pi/4}}{\sqrt{2\pi(1+M_0)k_1^*}}\left[1-\sqrt{\frac{2}{1+y_1^*}}-(1-\mathrm{i})E\big(2\overline{\mu}(1-y_1^*)\big)\right]\mathrm{e}^{\mathrm{i}(1-M_0)\overline{\mu}(1+y_1^*)}$$

with $k_1^*=\omega c/(2U_0)$, $\overline{\mu}=M_0k_1^*/\beta^2$. y_1^* is the chordwise coordinate made dimensionless by the half chord, E is the Fresnel integral

$$\mathrm{E}(\xi)=\int_0^{\xi}\frac{\mathrm{e}^{\mathrm{i}t}}{\sqrt{2\pi t}}\,dt$$

and $\tilde{w}$ is the upwash amplitude of the gust. The quantity $\ell(y_1^*)$ provides a consistent description of the source amplitude and phase distributions on the flap. It features an inverse-square root singularity at the leading edge. The latter is integrable and has been removed by replacing the continuous distributions by a set of discrete dipoles of finite amplitudes. In standard applications of Amiet's theory $\ell(y_1^*)$ is considered along the chord line of angle α_f (see Fig. 9). According to classical linearized theories of unsteady aerodynamics it can also be displaced on the mean-camber line of the flap, of angle α_{LE} at the leading edge, as long as the camber remains moderate. This modifies the orientation of the equivalent dipoles.

First computations based on the 2D model and on the transposed 3D model according to Oberai's transposition formula, Eq. (6), are compared in Fig. 10, where directivity diagrams are reported for various observer distances from the edge. In all plots the amplitude is scaled by the distance for an easier comparison. The parameters are representative of a real aircraft. The polar plots have their origin on the scattering edge so that the flap is shifted towards the negative angles; as a result the lobes are artificially distorted with respect to what would appear with a more conventional origin taken at the leading-edge of the flap. The chord length is 0.4 m. Oberai's transposition formula, Eq. (6), is found fully relevant for non-dimensional distances larger than $kr=16$ at the frequency of 500 Hz (note that the relative lobe expansion in Fig. 10(a) at $kr=8$ is caused by the relative proximity of the flap). At the higher tested frequency of 1 kHz, Oberai's transposition is found relevant only for $kr=32$. This value is retained as an acceptable threshold for validating the transposition. In typical small-scale wind-tunnel testing of a HLD mock-up scaled to 1/10, with the realistic Mach number value of 0.2 and the microphone distance of

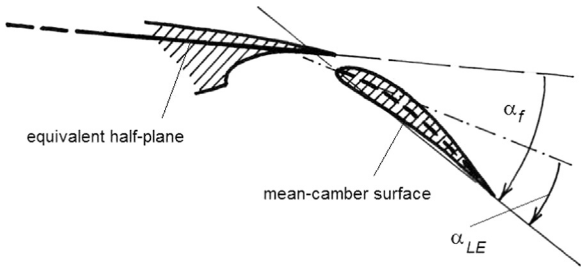

Fig. 9. Typical wing-flap configuration representative of landing conditions. Straight lines: half-plane approximation of the wing and mean-camber flap surface.

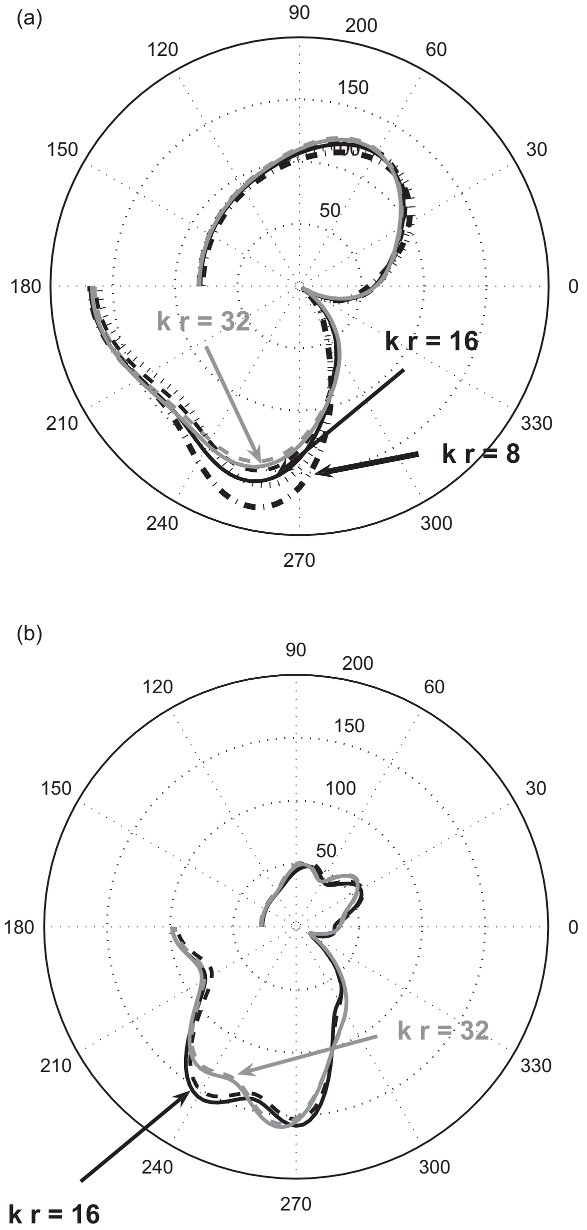

Fig. 10. Flap-noise directivity patterns with wing scattering, for various edge-observer distances. Corrected 2D calculation (—) versus 3D calculation (- - -). No Kutta correction. Mach number 0.35. (a) 500 Hz; (b) 1000 Hz. Chord length $c=0.4$ m, leading-edge distance to the edge $(x_0, y_0)_{LE} = (-0.05\ \text{m}, 0.07\ \text{m})$, flap deflection angle 30°.

$r=2$ m, the condition $kr > 32$ is ensured above a frequency of 800 Hz, representative of 80 Hz at full size. Significant errors are expected at even lower frequencies if two-dimensional models or simulations are compared with measurements.

Fig. 11 compares the total 3D field in the presence of the scattering edge with the free field at different frequencies, for the same basic parameters as in Fig. 10. The distance to the edge is set to $kr=16$ for 63 Hz and 250 Hz, and to $kr=32$ for 500 Hz and 1000 Hz to ensure satisfactory geometrical far-field conditions with respect to the volume of fluid embedding the flap and the edge. The calculations are repeated for two symmetrical positions of the flap leading edge, either 5 cm upstream (grey) as in the reference case of Fig. 10 or 5 cm downstream (black) of the scattering edge, and for the same vertical distance. Edge scattering starts to force the cardioid pattern below 250 Hz in this example, as shown by Fig. 11a and b. According to the asymptotic trend of point dipoles discussed in Section 2.2, the amplitude of the sound field also increases significantly (Fig. 11a). At 1000 Hz in Fig. 11d, the free field and the edge-scattered field coincide when the flap is shifted downstream. In contrast both diagrams significantly differ when the flap is shifted upstream. The net effect is an enhanced radiated sound towards the ground around the angles -110° to -115° and some reduction in the opposite directions. This is attributed to the masking-and-reflection effect on the dominant flap sources, caused by the overlap between the flap leading edge and the wing trailing edge. It is worth noting

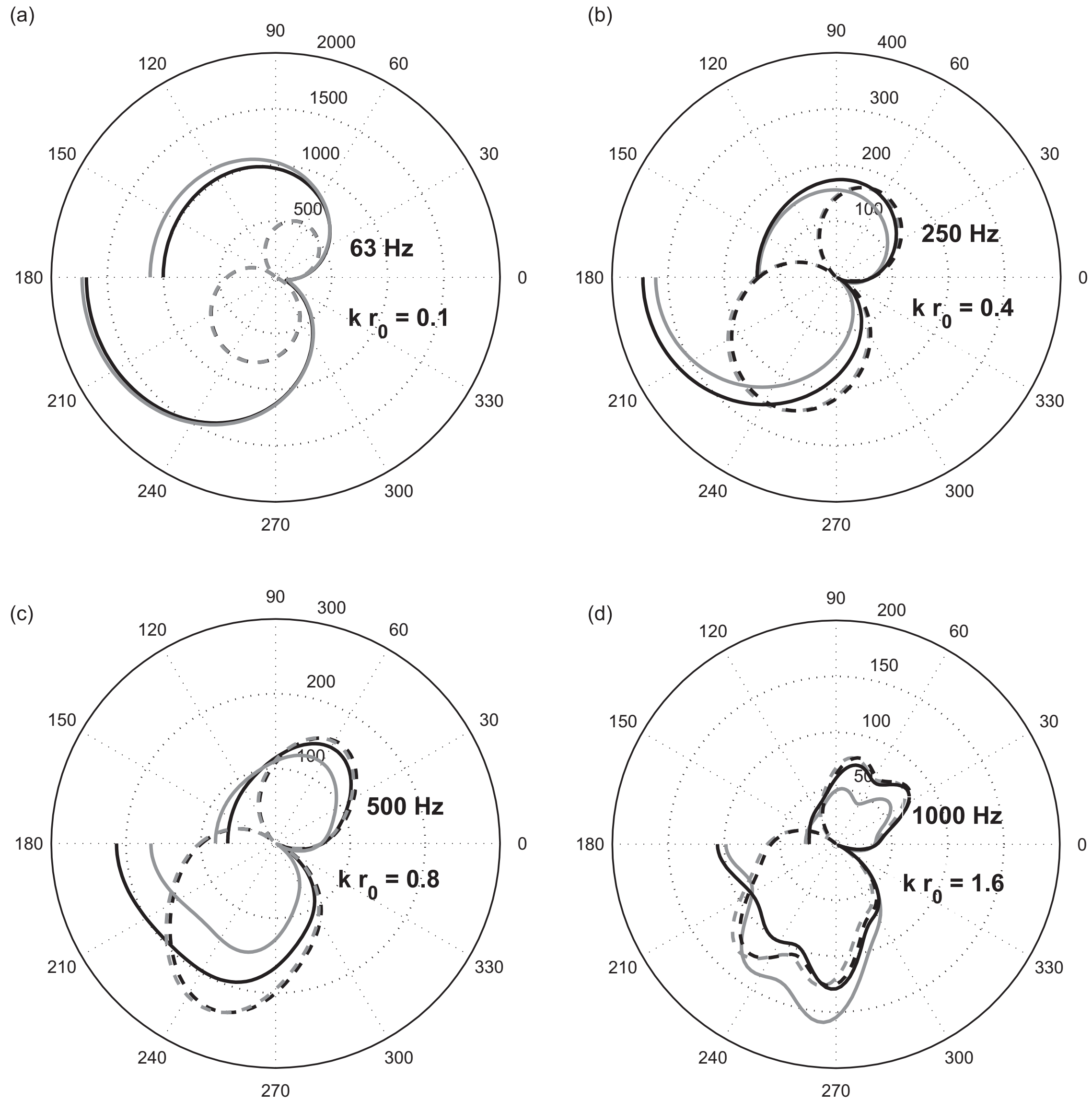

Fig. 11. Flap-noise directivity patterns of a deployed flap at various frequencies according to free-field radiation (- - -) or including the 3D model of wing scattering (—). No Kutta correction. Dimensionless gap size indicated on the plots. Mach number 0.35. Chord length $c = 0.4$ m, flap deflection angle 30°. Edge distance $kr = 16$ ((a) and (b)); $kr = 32$ ((c) and (d)). $x_0 = -5$ cm (grey) and $x_0 = +5$ cm (black).

that because of the inverse-square root singularity the leading-edge sources experience more pronounced scattering than sources distributed farther downstream. At 500 Hz (Fig. 11c), the scattering is responsible for a different directivity: the main lobe around $-130°$ is shifted below the screen and focuses upstream. At the same time the sound radiation is globally reduced, especially in the case of the overlap. In usual configurations of a deployed flap and at low frequencies for which the non-dimensional distance is smaller, the presence of the wing makes more sound expected to radiate toward the ground and in the upstream direction. Wing-scattering affects the frequency distribution of flap noise depending on the radiation angle, or equivalently depending on the precise location of the observer. The present calculations exhibit intermediate behaviours between the free-field radiation of an airfoil in a turbulent flow and the low-frequency cardioid approximation. This makes the derivations based on the exact Green's functions crucial for a correct modeling of the scattering effect.

3. Scattering by a rigid corner

This section is dealing with localized aeroacoustic phenomena at the corners of a flap side-edge. The formation of vortical patterns from the corners and the associated sound radiation have been addressed by vortex methods and numerical

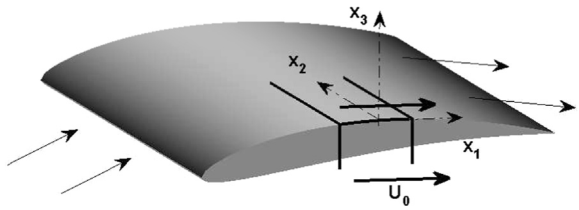

Fig. 12. Flap side-edge sketch and equivalent corner reference frame.

approaches (see for instance [28,29] and more recently [30]). The present work provides a complementary view based on the use of the corner Green's function.

- Preliminary considerations on the source-to-corner distance are given in Section 3.1.
- The exact Green's function for a stationary propagation medium is detailed in Section 3.2.
- A sample implementation is presented in Section 3.3.
- The asymptotic regime for a far-field observer and a source close to the corner is investigated in Section 3.4.
- The effect of a uniform flow is finally considered in Section 3.5.

3.1. Flap side-edge noise – preliminaries

Side edges of lifting surfaces such as high-lift flaps exhibit two corners, on the pressure side and the suction side, as depicted in Fig. 12. Free shear layers detach from the corners before rolling up and merging to form a structured tip vortex. This complicated flow is unsteady and fully three-dimensional with varying features along the chord, as thoroughly described by Angland [34] and Brooks and Humphreys [20], for instance. At relatively low and moderate frequencies in the sense that $kh \ll 1$ where h is the thickness of the flap, the side-edge behaves like the edge of a large plate of very small thickness. The physics is similar to that of trailing-edge noise except that the surrounding uniform flow is parallel to the side-edge instead of being perpendicular. The equivalent sources are convincingly interpreted as dipoles defined by the unsteady pressure jump between the pressure side and the suction side and radiating in free space, following Ffowcs Williams and Hawkings' statement of the analogy [20]. This first asymptotic view holds for the large-scale oscillatory motion of the tip vortex. That motion dominantly contaminates the aft region of the flap, near the tip/trailing-edge corner. Oppositely the initial small-scale oscillations of the shear layers that take place close to the side-edge corners are a high-frequency motion for which $kh > 1$. In this case both corners tend to decouple. Vortex dynamics developing in the very vicinity of one corner is not significantly influenced by the other corner which is quite far away in terms of aerodynamic wavelengths. For this other asymptotic regime, the dominant physics is interpreted as equivalent scattering of quadrupoles by a rigid corner of infinite sides according to Lighthill's original point of view. Of course this interpretation only makes sense for sources such that $kr_0 \ll 1$.

High-lift device noise is also analyzed from the standpoint of a distant observer. Therefore Green's function needs to be considered only in the limit of a source in the acoustic near field of the corner and an observer in the acoustic far field such that $k\hat{r} \gg 1$. Now the flight Mach number of an aircraft in approach can reach 0.3, suggesting that sound convection effects must be included in the analysis for physical consistency. Within the scope of a simplified analytical approach, this is achieved by assuming a uniform flow of some Mach number M_0 aligned with the edge of the corner, along the direction x_1 according to the sketch in Fig. 12 and by considering Green's function for the convected Helmholtz equation. Note that Cartesian coordinates will be preferred when uniform flow is considered (Section 3.5).

3.2. Wedge and corner Green's functions

Green's function of the space limited by a wedge for the Helmholtz equation, referred to as the wedge Green's function, has been derived first by MacDonald [14] in spherical coordinates in the case of rigid walls, for source and observer located in the same plane normal to the wedge. Another expression for soft walls and arbitrary source–observer configurations has been derived by Mel'nik and Podlipenko [31]. The case of the rigid wedge with arbitrary source and observer locations is obtained by combining both. As seen in Fig. 13 for the corner ($\Phi = 3\pi/2$), the source and observer coordinates are $(\hat{r}_0, \Theta_0, \phi_0)$ and $(\hat{r}, \Theta, \phi)$, respectively. MacDonald's formulation assumes $\Theta_0 = \Theta = \pi/2$.

Green's function for a rigid wedge with an apex angle Φ reads

$$G(\mathbf{x}, \mathbf{x}_0) = \frac{-\pi \mathrm{i}}{4\Phi\sqrt{\hat{r}\hat{r}_0}} \sum_{m=0}^{\infty} \varepsilon_m \cos\left(m'\phi_0\right) \cos(m'\phi) \sum_{\kappa=0}^{\infty} (2m' + 4\kappa + 1) \frac{\Gamma(2m' + 2\kappa + 1)}{\Gamma(2\kappa + 1)}$$
$$\times P_{m'+2\kappa}^{-m'}(\cos\,\Theta_0) P_{m'+2\kappa}^{-m'}(\cos\,\Theta) J_{m'+2\kappa+1/2}(kr_<) H_{m'+2\kappa+1/2}^{(1)}(kr_>), \tag{9}$$

where ε_m is 1 for $m=0$ and 2 for $m > 1$ [13], $0 < \Phi < 2\pi$ and $m' = m\pi/\Phi$. $P_{m'+2\kappa}^{-m'}$ is the general Legendre function. J_υ and $H_\upsilon^{(1)}$

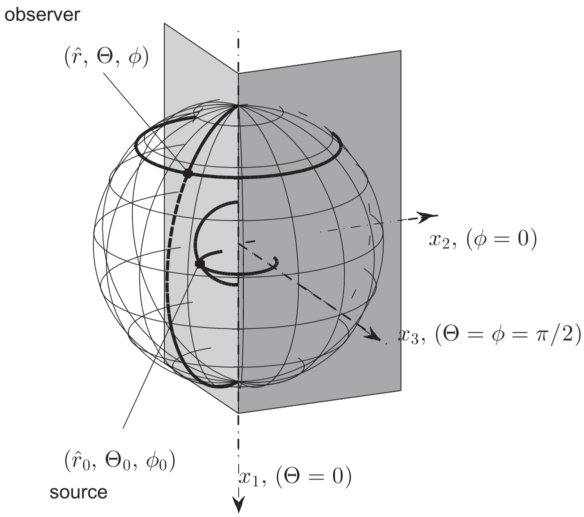

Fig. 13. Cartesian and spherical reference frames attached to a corner, with arbitrary source and observer locations. Parallel-and-meridian mesh shown for clarity.

are the Bessel and Hankel functions of the first kind and of order υ, respectively. Depending on relative source and observer locations, $r_> = \max(\hat{r}, \hat{r}_o)$ and $r_< = \min(\hat{r}, \hat{r}_o)$.

The geometrical expansion of the Legendre function $P_{m'+2\kappa}^{-m'}(\cos\Theta)$

$$P_{m'+2\kappa}^{-m'}(\cos\Theta) = \frac{2^{1-m'}(\sin\Theta)^{-m'}}{\sqrt{\pi}\Gamma(1/2-m')} \times \sum_{n=0}^{\infty} \frac{\Gamma(n+1/2-m')\Gamma(2\kappa+n+1)}{\Gamma(n+1)\Gamma(2\kappa+n+m'+3/2)} \sin[(2n+1+2\kappa)\Theta] \tag{10}$$

is used in the paper for the computations [21].

Taking Φ in Eq. (9) as $3\pi/2$ provides the corner Green's function as

$$G(\mathbf{x}, \mathbf{x}_0) = \frac{-\mathrm{i}}{6\sqrt{\hat{r}\hat{r}_o}} \sum_{m=0}^{\infty} \varepsilon_m \cos(2m\phi_0/3)\cos(2m\phi/3) \times \sum_{\kappa=0}^{\infty} (4m/3+4\kappa+1)\frac{\Gamma(4m/3+2\kappa+1)}{\Gamma(2\kappa+1)}$$

$$\times P_{2m/3+2\kappa}^{-2m/3}(\cos\Theta_0) P_{2m/3+2\kappa}^{-2m/3}(\cos\Theta) J_{2m/3+2\kappa+1/2}(kr_<) H_{2m/3+2\kappa+1/2}^{(1)}(kr_>). \tag{11}$$

3.3. Scattered field of a quadrupole

For the sake of validation, analytical results for simple point sources in a quiescent medium at a single frequency are compared with numerical simulations in this section. The reference numerical solution is obtained from a commercial Boundary-Element Method (BEM) solver LMS Virtual Lab. The solver is known to be able to handle diffraction problems for unbounded domains [32]. Since the BEM technique requires at least 10 mesh points per wavelength, the tests are performed at two reasonably low frequencies with regards to the configuration. A lateral quadrupole and a longitudinal quadrupole with axes along the radial direction are tested. The quadrupoles are located at $(1.24\lambda, \pi/2, \pi/4)$, with the source strength $Q(\omega) = (0.01 + \mathrm{i}0.01)$ kg m^2/s^2. In order to minimize the effect of the free ends of the computational domain along the direction $\Theta = 0$, the corner is featured by two flat plates of size $7\lambda \times 7\lambda$ and the radiated field is considered in the mid plane at $\Theta = \pi/2$. The total number of acoustic elements is equal to 7200. The size of the quadrilateral elements, $l_{\max} \approx 0.06\lambda$ at the first frequency, is satisfying the BEM criteria [33]. The directivity diagrams of the two quadrupole-corner configurations are plotted in Fig. 14a and b. The line and symbols stand for the analytical and BEM predictions, respectively, at a distance of 3λ from the corner. The very good agreement validates the implementations. For both quadrupoles, the discrepancies between the analytical and numerical results are less than 1 dB. They are attributed to the domain truncation inherent to the numerical method.

In order to avoid mathematical complexity, the present investigation is split into two steps. A parametric analysis is first performed on Green's function with no flow in order to determine the range of practical values of the parameters $k\hat{r}_0$ and $k\hat{r}$ for which the asymptotic regime is ensured. In a second step the effect of uniform flow is introduced in the asymptotic Green's function only.

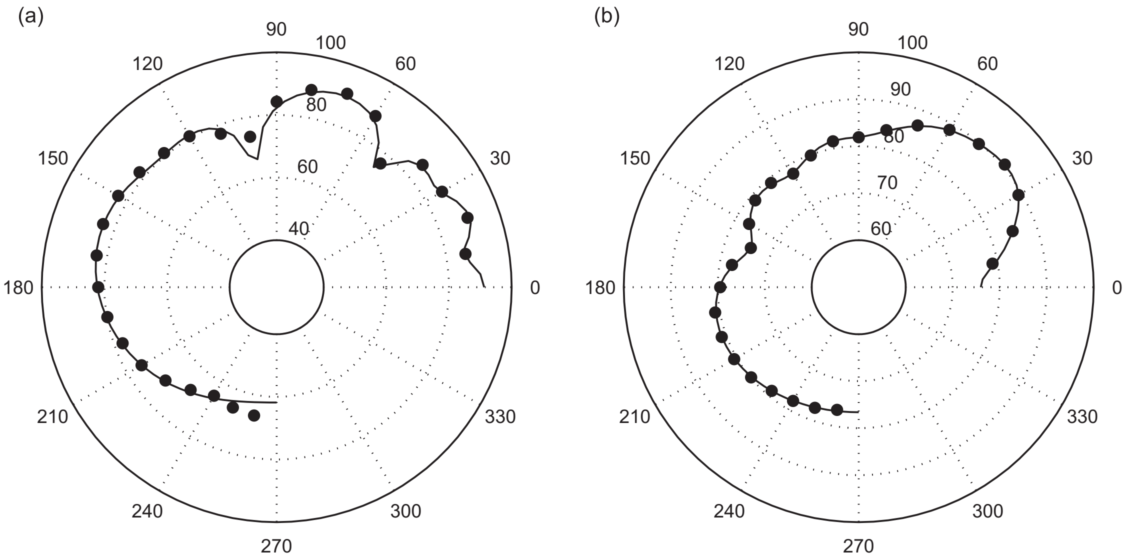

Fig. 14. Directivity patterns of lateral (a) and longitudinal (b) quadrupoles in the vicinity of a corner. Sound levels in dB. Analytical model (—) versus BEM results (- · -). Source coordinates $(\hat{r}_0, \Theta_0, \phi_0) = (1.24\lambda, \pi/2, \pi/4)$; observer distance 3λ.

3.4. The asymptotic regime

Accounting for a source located in the immediate neighborhood of the wedge, $k\hat{r}_0 \ll 1$, and for a far-field observer, $k\hat{r} \gg 1$, the Bessel and Hankel functions can be replaced by their asymptotic forms [21]:

$$J_{m'+2\kappa+1/2}(k\hat{r}_0) \sim \sqrt{\frac{2k\hat{r}_0}{\pi}}(2k\hat{r}_0)^{m'+2\kappa+1/2}\frac{\Gamma(m'+2\kappa+1)}{\Gamma(2m'+4\kappa+2)},$$
$$H^{(1)}_{m'+2\kappa+1/2}(k\hat{r}) \sim -\mathrm{i}\sqrt{\frac{2}{\pi k\hat{r}}}\,\mathrm{e}^{\mathrm{i}k\hat{r}}\,\mathrm{e}^{-\mathrm{i}(m'+2\kappa)\pi/2}. \tag{12}$$

Furthermore the $\kappa = 0$ term of Eq. (9) obviously dominates and the other terms can be discarded [13]. Therefore, combining the asymptotic definitions Eq. (9) becomes

$$G(\mathbf{x}, \mathbf{x}_0) = \frac{-\mathrm{e}^{\mathrm{i}k\hat{r}}}{2\hat{r}}\sum_{m=0}^{\infty}\varepsilon_m \cos(m'\phi_0)\cos(m'\phi)P_{m'}^{-m'}(\cos\Theta_0)P_{m'}^{-m'}(\cos\Theta) \times (2k\hat{r}_0)^{m'}\Gamma(m'+1)\,\mathrm{e}^{-\mathrm{i}m'\pi/2}. \tag{13}$$

The decrease of sound with observer distance for a point monopole located at the dimensionless distance to the wedge $k\hat{r}_0 = 0.1$ is plotted in Fig. 15. The source and observer angles are $\phi_0 = \pi/6$ and $\phi = 5\pi/4$, respectively, with $\Theta_0 = \Theta = 0$. The strength of the monopole is selected as $q(\omega) = (0.01 + \mathrm{i}0.01)$ kg/s^2. The solid and dashed lines stand for the exact analytical solution, Eq. (11), and the asymptotic formulation, Eq. (13), respectively. Both solutions nearly coincide above $k\hat{r} = 3$, where the far-field decay $1/\hat{r}$ is reached. The same test for a longitudinal quadrupole is also reported in Fig. 15. The strength of the quadrupole is again $Q(\omega) = (0.01 + \mathrm{i}0.01)$ kg m^2/s^2 and the plot is shifted down by 90 dB for the sake of comparison. Both the exact and asymptotic solutions are now found to converge beyond the indicative threshold $k\hat{r} = 20$.

Eq. (13) still includes a summation over all mode orders m. Since spatial derivatives with respect to source coordinates will be applied with the constraint $k\hat{r}_0 \ll 1$ in the asymptotic regime, the field will be dominated by the smallest orders leading to negative values of $m' - 1$. Therefore, only $m=0$ and $m=1$ need to be retained in Eq. (13). Now $P_0^0(\cos\Theta) = 1$, and

$$P_\nu^{-\nu}(\cos\Theta) = \frac{2^{-\nu}[\sin\Theta]^\nu}{\Gamma(\nu+1)}.$$

Finally the expression of the asymptotic Green's function follows as $G = G_0 + G_1$, with

$$G_0(\mathbf{x}, \mathbf{x}_0) = \frac{-\mathrm{e}^{\mathrm{i}k\hat{r}}}{3\pi\hat{r}},$$
$$G_1(\mathbf{x}, \mathbf{x}_0) = \frac{-2\mathrm{e}^{\mathrm{i}(k\hat{r}-\pi/3)}\,(k\hat{r}_0)^{2/3}}{3\pi\hat{r}2^{2/3}\Gamma(5/3)}\cos(2\phi_0/3)\,\cos(2\phi/3)[\sin\Theta_0]^{2/3}[\sin\Theta]^{2/3}. \tag{14}$$

For source and observers located in the plane $\Theta_0 = \Theta = \pi/2$, the expressions still reduce to the ones given in the references [35,13] and can be seen as a complete 3D extension of the latter.

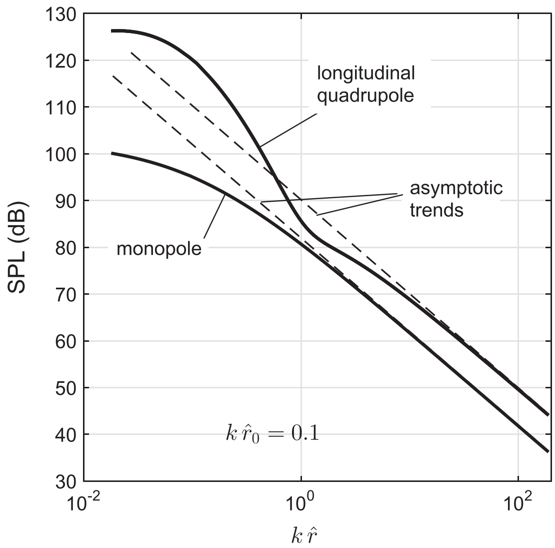

Fig. 15. Near-field to far-field sound pressure level decrease of a monopole and of a longitudinal quadrupole located nearby a corner. $k\hat{r}_0 = 0.1$. Exact (—) and asymptotic (- - -) solutions.

3.5. Effect of uniform flow – application to flap side-edge noise

As the uniform flow induces anisotropy, the physics is better addressed in Cartesian coordinates (x_1, x_2, x_3), with x_1 along the flow direction $(\Theta = 0)$ and x_2 along the direction normal to the edge $(\phi = 0)$. Because the boundary conditions of the Helmholtz problem in the presence of the corner are independent of the coordinate x_1 along the edge, the effect of a uniform flow is simply included in the analysis by performing the same change of variable as used in Section 2.2 for the scattering by a trailing edge. The present case is simpler in the sense that no Kutta condition needs to be considered. Green's function with flow G_{M_0} is obtained from the one in a stationary medium G by the formula

$$G_{M_0}(\mathbf{x}, \mathbf{x}_0, k) = \frac{1}{\beta} G(\mathbf{x}, \mathbf{Y}, K)\, \mathrm{e}^{\mathrm{i}KM_0(X_1 - Y_1)} \tag{15}$$

with $(X_1, Y_1) = (x_1, y_1)/\beta$, $K = k/\beta$, $\beta = \sqrt{1 - M_0^2}$. $\mathbf{x} = (X_1, x_2, x_3)$ and $\mathbf{Y} = (Y_1, y_2, y_3)$ stand for the observer and source coordinate vectors, respectively. Eq. (15) applies to both exact and asymptotic Green's functions. Only the latter is addressed here. It is worth noting that when calculating the double gradient with respect to source coordinates, the terms corresponding to $\cos(2\phi_0/3)$ are not affected by the flow.

The asymptotic Green's function with flow reads, combining spherical and Cartesian coordinates for convenience,

$$G_{M_0}(\mathbf{x}, \mathbf{x}_0) = -\frac{\mathrm{e}^{\mathrm{i}k(S_0 + M_0 x_1)/\beta^2}}{4\pi S_0} - \frac{2^{-2/3}\, \mathrm{e}^{-\mathrm{i}\pi/3}\, \mathrm{e}^{\mathrm{i}k(S_0 + M_0 x_1)/\beta^2}}{\pi S_0 \Gamma(2/3)} \times \cos(2\phi_0/3)\cos(2\phi/3) \left[\frac{\sqrt{x_2^2 + x_3^2}}{S_0}\right]^{2/3} \left[k\sqrt{y_2^2 + y_3^2}\right]^{2/3}, \tag{16}$$

with $S_0 = \left[x_1^2 + \beta^2(x_2^2 + x_3^2)\right]^{1/2}$. The cosine terms of angles ϕ and ϕ_0 only involve coordinates (x_2, x_3) and (y_2, y_3). The final expression exhibits the property

$$\frac{\partial G_{M_0}}{\partial y_1} = \frac{\partial^2 G_{M_0}}{\partial y_1^2} = 0.$$

Therefore dipole or quadrupole components aligned with the streamwise direction will produce no scattering, as expected.

The far-field directivity of the sound field is determined by Green's function *via* the observer coordinates, whereas the amplitude is determined by the source parameters only. Introducing the emission angle $\overline{\theta}_0$ such that

$$\cos\overline{\theta}_0 = \frac{x_1}{S_0}, \quad \sin\overline{\theta}_0 = \frac{\beta\sqrt{x_2^2 + x_3^2}}{S_0}$$

leads to the expression of the directivity function

$$D(\mathbf{x}) = -\frac{\mathrm{e}^{\mathrm{i}(k/\beta^2)S_0[1 + M_0\cos\overline{\theta}_0]}}{(2\beta)^{2/3}\pi S_0 \Gamma(2/3)}\, \mathrm{e}^{-\mathrm{i}\pi/3} \cos\left(\frac{2\phi}{3}\right)\left[\sin\overline{\theta}_0\right]^{2/3}.$$

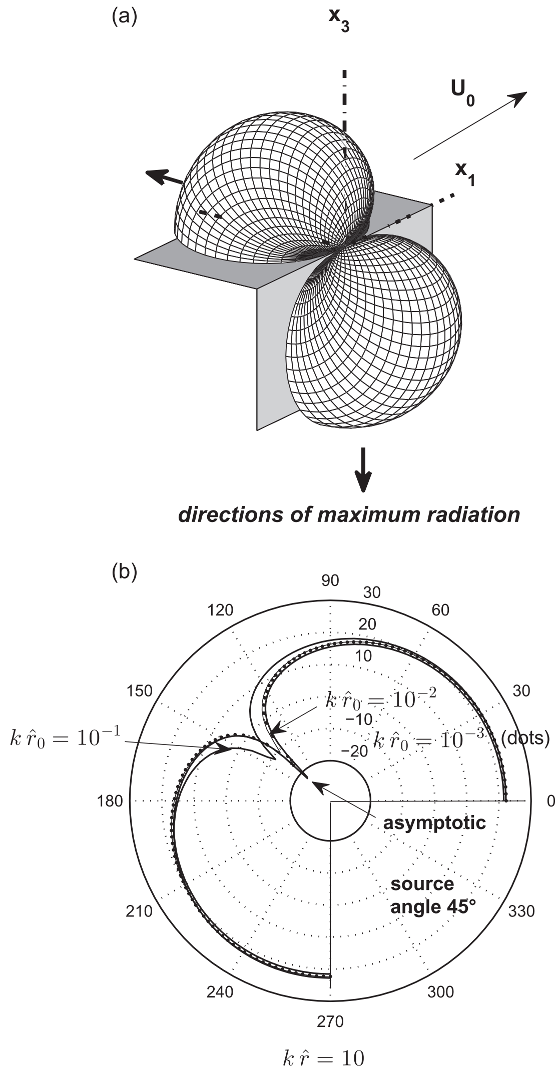

Fig. 16. (a) Directivity pattern of the sound from a source close to a rigid corner: asymptotic regime. (b) Directivity diagrams in the plane $\Theta = \pi/2$ as a function of the source-edge distance, according to the exact and asymptotic formulations, for a longitudinal quadrupole Q_{rr}. Sound pressure level scaled by the factor $(k\hat{r}_0)^{-4/3}$. $M_0 = 0$.

This function is plotted in Fig. 16a. It is found that in the asymptotic regime radiation goes to zero at the angle $\phi = 3\pi/4$. The same trend would be followed by any kind of source because it is imposed by Green's function itself. As a result the initial shear-layer oscillations developing from the pressure-side corner of a flap side-edge radiate no sound at the side-line angle of 45° from the vertical (fly-over) plane. Because of the factor $\sin\overline{\theta}_0$, no sound is radiated along the direction of the corner line that is moderately inclined with respect to the flight-path direction for an aircraft. Even in the presence of uniform flow symmetrical sound amplitudes are radiated upstream and downstream, which is typical of equivalent dipole sources perpendicular to the flow direction. The maximum sound is radiated along the sides of the corner, normal to the edge. These features are similar to the cardioid pattern of the asymptotic Green's function for the edge of a rigid half-plane, characteristic of trailing-edge noise sources (Section 2).

The amplitude is given by the term $Q_{ij}\partial^2 G/\partial y_i\,\partial y_j$ with summation on the indices 2 and 3 only. The double space derivatives of the leading term $(kr_0)^{2/3}$ of Green's function with $r_0 = \sqrt{y_2^2 + y_3^2}$ make an expected amplification scaling as $(kr_0)^{-4/3}$. The amplification is less pronounced than that reported by Ffowcs Williams and Hall, scaling as $(kr_0)^{-3/2}$, in the similar problem of quadrupole sound scattering by the edge of a half plane [3]. It is worth noting that for shear layers detaching from the corners of a side-edge, the fluctuating velocity components are precisely large in the directions y_2 and y_3 and small along y_1.

In the amplified asymptotic regime the sound level at large distances is expectedly constant when scaled by the factor $(kr_0)^{-4/3}$. This is checked in Fig. 16b, where the directivity as deduced from the exact solution is computed for small source-to-corner distances. All scaled plots tend to collapse and coincide with the theoretical dependence $\cos(2\phi/3)$ as the source

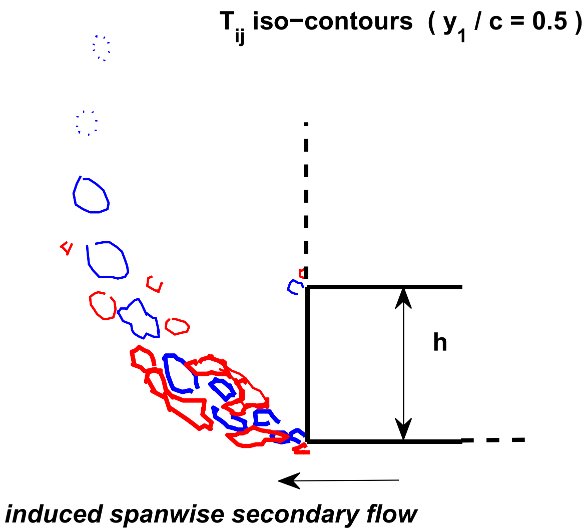

Fig. 17. Qualitative iso-contour structure of Lighthill's stress tensor around a flap side-edge at high frequency, showing dominant contribution from the lower corner. Plots in a plane normal to main flow direction U_0, at 50 percent chord. Reproduced from reference [36].

parameter kr_0 vanishes. The results suggest that the asymptotic regime is entered when $kr_0 < 0.1$. This means that quadrupole sources located farther away from the corner nearly radiate with the same efficiency as in free field, experiencing no amplification. As such they do not contribute significantly to the sound field at low Mach numbers because they remain much smaller than dipole sources distributed elsewhere. In contrast quadrupoles in the very vicinity of the corner are amplified. Their quadrupole nature is overwhelmed by the scattering process which produces more efficient dipole-like radiation.

The same discussion holds as well for the disturbances originating from the upper (suction-side) corner, at the price of a change of axes. Therefore that contribution radiates significant sound in the aforementioned side-line direction. But both corners do not produce identical flows at the same chordwise location, as suggested by flap-side edge flow and noise investigations reported in the literature [36]. A typical distribution of Lighthill's stress tensor T_{ij} in a plane normal to the side-edge at 50 percent chord according to numerical simulations is plotted as iso-value contours in Fig. 17, from Streett [36]. A high-amplitude quadrupole field is developing from the lower corner where the flow separates mainly because of the spanwise outboard secondary flow from the flap pressure side. In contrast the secondary vortex sheet starting from the upper corner is very weak. More generally the local contributions along the chord line depend on the relative states of the separating shear layers, as well as on the angle of attack of the flap. As a consequence the lower corner is expected to produce the highest contribution to the sound in the example. More precisely the dominant sound comes from the parts of T_{ij} close enough to the corner to enter the asymptotic regime characterized by amplification. For this contribution at sufficiently high frequencies and for observer locations facing the pressure side, ignoring the effect of the upper corner and resorting to the present Green's function makes sense.

The expected extinction at 45° is indeed observed, at least qualitatively, in the computations by Streett [36] at very high frequencies. In contrast the author also reports a cardioid directivity pattern in a plane $x_1 = 0$ normal to the flap and containing the span at lower frequencies. No mention of the Helmholtz number kh is made in the referenced paper, hence no precise bounds can be defined for the asymptotic regime. Nevertheless the present analysis is believed to hold at least within a small circle around the bottom corner of the plot of Fig. 17.

It must be noted that the boundary layers developing on the pressure side of a flap also possibly carry small-scale turbulence that is convected in the spanwise direction over the corner, independent of any other disturbances developing in the free shear-layers. Noise radiation similar to trailing-edge noise is expected to take place for this boundary-layer turbulence. This aspect of flap side-edge noise could also be described using the present corner Green's function.

4. Conclusion

Exact Green's functions for the Helmholtz equation and for rigid half-plane and wedges have been implemented from the literature and used in this work, in order to highlight fundamental aspects of sound diffraction by edges and corners in high-lift devices. This could also be used for jet–wing interaction problems. Furthermore the effect of uniform fluid motion has been included in the formulations. In most cases and for both configurations fluid motion only causes distortions without fundamental changes in the general physics, at least for the moderate Mach numbers of interest in the technology of high-lift devices.

In the case of trailing-edge scattering the relative flow direction is considered normal to the edge. Both the exact half-plane Green's function and its asymptotic reduction for a source very close to the edge in terms of acoustic wavelengths have been investigated. The main outcomes are listed below.

- The characteristic radiation pattern of the asymptotic regime is a cardioid, with zero sound in the wake and maximum sound in the opposite direction. The regime is continuously approached when progressively reducing the source Helmholtz number kr_0; it typically holds for $kr_0 < 0.1$ for both dipoles and quadrupoles and corresponds to a strong amplification, with phase opposition between both sides of the half-plane.
- The Kutta condition still significantly enhances the acoustic radiation in this regime. The effect increases with the Mach number.
- Both effects expectedly play a role in the scattering of flap noise by the wing of an aircraft for the first third-octave bands involved in the calculation of the EPNL (Effective Perceived Noise Level used to quantify the noise exposure around airports).
- When the observer is moved to the far field and for small values of kr_0 Green's function reduces to the simple closed-form expression used in the literature of trailing-edge noise.
- The main features of the scattered fields in the two-dimensional and three-dimensional formulations are identical. A classical transposition formula relating the former to the mid-span plane reduction of the latter in the far field has been extended to account for the effect of mean flow. It is shown to be valid for Helmholtz numbers based on the observer distance beyond $kr = 30$.

The exact Green's function for the rigid corner in a medium at rest has been implemented and extended to account for the presence of a mean flow. In this case the mean flow is assumed uniform and parallel to the wedge. The formulation has also been specified in the asymptotic regime of a near-field source and a far-field observer. This simplification is relevant to investigate the high-frequency flap side-edge noise generated by initial oscillations of the shear layers detaching from the side-edge corners, during approach and landing operation. The main results are as follows.

- The asymptotic sound radiation again involves strong amplification of the equivalent quadrupoles as typically $kr_0 \le 0.1$. In this regime the radiation is maximum normal to the edge along the sides of the corner and exactly zero along the bisectrix of the corner apex angle.
- The asymptotic analysis is reliable whenever the conditions $kr_0 \ll 1$ and $kh > 1$ are fulfilled together, with h being the flap thickness. It is more likely to make sense in the modern very large aircraft architectures, for oblique side-line radiation.
- The amplification means that the radiation efficiency of the sources increases, in other words that their equivalent polar order is reduced by one unit. This general property is similarly pointed out by Howe [2] using the formalism of compact Green's functions.

The present exact formulations of Green's functions for the Helmholtz equation cover all possible configurations. In particular they are the only relevant way of quantifying the sound in the shadow region of simple obstacles. They also provide reference solutions, dedicated to the validation of numerical simulations, on the one hand, and to the assessment of the validity range of simpler, asymptotic formulations, on the other hand.

Acknowledgement

This work has been partially supported by the FP7 Collaborative Project ECOQUEST (Grant agreement no. 233541) and by the industrial Chair ADOPSYS co-financed by SAFRAN-Snecma and the French Agence Nationale de la Recherche.

Appendix A. Implementation of the integrals

A.1. Splitting formulae

All components of the first and second gradients of the three-dimensional half-plane Green's function involve the same infinite-bound integrals with derivatives of K_1^* in the integrands. Classical relationships between modified Bessel functions and their derivatives can be used to reduce the integrals. From [21]

$$K_1^{*\prime}(\mathrm{i}\xi) = K_0^*(\mathrm{i}\xi) + \frac{\mathrm{i}}{\xi} K_1^*(\mathrm{i}\xi); \quad K_0^{*\prime}(\mathrm{i}\xi) = K_1^*(\mathrm{i}\xi);$$

$$K_1^{*\prime\prime}(\mathrm{i}\xi) = \frac{\mathrm{i}}{\xi} K_0^*(\mathrm{i}\xi) + \left(1 - \frac{2}{\xi^2}\right) K_1^*(\mathrm{i}\xi)$$

for any positive value of ξ, then

$$\int_{-\infty}^{\overline{u}_0} K_1^{*\prime}\left(\mathrm{i}K\overline{r}\sqrt{1+u^2}\right)\,\mathrm{d}u = \int_{-\infty}^{\overline{u}_0} K_0^{*}\left(\mathrm{i}K\overline{r}\sqrt{1+u^2}\right)\,\mathrm{d}u + \frac{\mathrm{i}}{K\overline{r}}\int_{-\infty}^{\overline{u}_0} \frac{K_1^{*}\left(\mathrm{i}K\overline{r}\sqrt{1+u^2}\right)}{\sqrt{1+u^2}}\,\mathrm{d}u$$

and

$$\int_{-\infty}^{\overline{u}_0} K_1^{*\prime\prime}\left(\mathrm{i}K\overline{r}\sqrt{1+u^2}\right)\sqrt{1+u^2}\,\mathrm{d}u = \frac{\mathrm{i}}{K\overline{r}}\int_{-\infty}^{\overline{u}_0} K_0^{*}\left(\mathrm{i}K\overline{r}\sqrt{1+u^2}\right)\,\mathrm{d}u + \int_{-\infty}^{\overline{u}_0} K_1^{*}\left(\mathrm{i}K\overline{r}\sqrt{1+u^2}\right)\sqrt{1+u^2}\,\mathrm{d}u - \frac{2}{K^2\overline{r}^2}\int_{-\infty}^{\overline{u}_0} \frac{K_1^{*}\left(\mathrm{i}K\overline{r}\sqrt{1+u^2}\right)}{\sqrt{1+u^2}}\,\mathrm{d}u.$$

Since equivalent expressions hold with $\overline{u}_1$ and $\overline{r}'$, this will not be repeated later on in the Appendix.

Noting that the integrands are symmetric functions, the following identity is useful for practical implementation [37]:

$$\int_0^{\infty} \frac{K_1^{*}\left(\mathrm{i}K\overline{r}\sqrt{1+u^2}\right)}{\sqrt{1+u^2}}\,\mathrm{d}u = -\frac{\pi}{2}\int_0^{\infty} \frac{H_1^{(1)}\left(K\overline{r}\sqrt{1+u^2}\right)}{\sqrt{1+u^2}}\,\mathrm{d}u = -\frac{\pi}{2}\int_0^{\infty} H_1^{(1)}(K\overline{r}\cosh\xi)\,\mathrm{d}\xi = \mathrm{i}\frac{\pi}{2}\frac{\mathrm{e}^{\mathrm{i}K\overline{r}}}{K\overline{r}}. \tag{17}$$

Similarly

$$\int_0^{\infty} K_0^{*}\left(\mathrm{i}K\overline{r}\sqrt{1+u^2}\right)\,\mathrm{d}u = \mathrm{i}\frac{\pi}{2}\frac{\mathrm{e}^{\mathrm{i}K\overline{r}}}{K\overline{r}}. \tag{18}$$

Furthermore, by identifying the formal derivatives of both sides of Eqs. (17) and (18) with respect to $\overline{r}$ or K, other formulae are obtained as

$$\int_0^{\infty} K_1^{*}\left(\mathrm{i}K\overline{r}\sqrt{1+u^2}\right)\sqrt{1+u^2}\,\mathrm{d}u = \frac{-\mathrm{i}}{K}\frac{\partial}{\partial\overline{r}}\int_0^{\infty} K_0^{*}\left(\mathrm{i}K\overline{r}\sqrt{1+u^2}\right)\,\mathrm{d}u = \frac{\mathrm{i}\pi}{2}\left(1+\frac{\mathrm{i}}{K\overline{r}}\right)\frac{\mathrm{e}^{\mathrm{i}K\overline{r}}}{K\overline{r}},$$
$$\int_0^{\infty} K_1^{*\prime}\left(\mathrm{i}K\overline{r}\sqrt{1+u^2}\right)\mathrm{d}u = \frac{\mathrm{i}\pi}{2}\left(1+\frac{\mathrm{i}}{K\overline{r}}\right)\frac{\mathrm{e}^{\mathrm{i}K\overline{r}}}{K\overline{r}}. \tag{19}$$

Finally

$$\int_0^{\infty} K_1^{*\prime\prime}\left(\mathrm{i}K\overline{r}\sqrt{1+u^2}\right)\sqrt{1+u^2}\,\mathrm{d}u = \frac{\mathrm{i}\pi}{2}\left[1+\frac{2\mathrm{i}}{K\overline{r}}-\frac{2}{K^2\overline{r}^2}\right]\frac{\mathrm{e}^{\mathrm{i}K\overline{r}}}{K\overline{r}}.$$

These identities allow splitting the infinite integrals into two parts, so that one of them has a closed-form expression whereas the remaining one must be computed numerically but is bounded.

A.2. Quadrature of bounded parts

Introducing the function $\overline{Q} = K\overline{r}\sqrt{1+u^2}$ for simplicity, the bounded parts of the integrals involving derivatives of the modified Bessel functions can be written in a convenient way for numerical implementation as

$$\int_0^{\overline{u}_0} K_1^{*\prime\prime}\left(\mathrm{i}K\overline{r}\sqrt{1+u^2}\right)\sqrt{1+u^2}\,\mathrm{d}u = \frac{1}{K\overline{r}}\int_0^{\overline{u}_0}\left\{-\mathrm{i}K_0\left(\mathrm{i}\overline{Q}\right)+K_1\left(\mathrm{i}\overline{Q}\right)\overline{Q}\left[1-\frac{2}{\overline{Q}^2}\right]\right\}^{*}\mathrm{d}u,$$
$$\int_0^{\overline{u}_0} K_1^{*\prime}\left(\mathrm{i}K\overline{r}\sqrt{1+u^2}\right)\,\mathrm{d}u = \int_0^{\overline{u}_0}\left\{K_0\left(\mathrm{i}\overline{Q}\right)-\frac{\mathrm{i}}{\overline{Q}}K_1\left(\mathrm{i}\overline{Q}\right)\right\}^{*}\mathrm{d}u.$$

Finally, routine instructions are only needed for the functions K_0 and K_1. It must be noted that because the integrands are even functions the negative bounds $\overline{u}_{0,1}$ can be replaced by their absolute values provided that the signs of the integrals are changed.

References

[1] M.J. Lighthill, On sound generated aerodynamically. I—General theory, *Proceedings of Royal Society of London, Series A*, 211 (1952).
[2] M.S. Howe, *Theory of Vortex Sound*, Cambridge Univ. Press, 2003.
[3] J.E. Ffowcs Williams, L.H. Hall, Aerodynamic sound generation by turbulent flow in the vicinity of a scattering half plane, *Journal of Fluid Mechanics* 40 (4) (1970) 657–670.
[4] M.S. Howe, The aerodynamic noise of a slot in an aerofoil, *ARC reports and memoranda*, no 3830, 1977.
[5] M.S. Howe, Aerodynamic sound generated by a slotted trailing edge, *Proceedings of Royal Society London series A*, 373 (1980) 235–252.
[6] J.E. Ffowcs Williams, D.L. Hawkins, Sound generated by turbulence and surfaces in arbitrary motion, *Proceedings of Royal Society of London Series A*, 264 (1151) (1969) 321–342.

[7] M. Khorrami, M.E. Berkman, M. Choudhari, Unsteady flow computations of a slat with a blunt trailing edge, *AIAA Journal* 38 (11) (2000) 2050–2057.
[8] M.R. Khorrami, B.A. Singer, M.E. Berkman, Time-accurate simulations and acoustic analysis of slat free-shear-layer, *AIAA Journal* 40 (7) (2002) 1284–1291.
[9] M. Terracol, E. Labourasse, E. Manoha, P. Sagaut, Simulation of the 3D unsteady flow in a slat cove for noise prediction. *Ninth AIAA/CEAS Aeroacoustics Conference and Exhibit*, paper 2003-3110, Hilton Head SC, 2003.
[10] S. Deck, Zonal-detached-eddy simulation of the flow around a high-lift configuration, *AIAA Journal* 43 (2005) 2372–2384.
[11] D. König, S.R. Koh, M. Meinke, W. Shröder, Two-step simulation of slat noise, *Computational Fluids* 39 (2010) 512–524.
[12] R. Satti, Y. Li, R. Shock, S. Noelting, Unsteady flow analysis of a multi-element airfoil using Lattice Boltzmann Method, *AIAA Journal* 50 (9) (2012) 1805–1816.
[13] A.D. Pierce, *Acoustics: An Introduction to Its Physical Principles and Applications*, Acoustical Society of America, New York, 1989, 250–312 (Chapter 6).
[14] H.M. Macdonald, A class of diffraction problems, *Proceedings London Mathematical Society* 14 (1915) 410–427.
[15] D.S. Jones, Aerodynamic sound due to a source near a half-plane, *Journal of the Institute of Mathematics and its Applications* 9 (1972) 114–122.
[16] S.W. Rienstra, Sound diffraction at a trailing edge, *Journal of Fluid Mechanics* 108 (1981) 443–460.
[17] M. Roger, S. Pérennès, Low-frequency noise sources in two-dimensional high-lift devices, *Sixth AIAA/CEAS Aeroacoustics Conference*, paper 2000-1972, Lahaina HA, 2000.
[18] M. Molin, M. Roger, S. Barré, Prediction of aircraft high-lift device nose using dedicated analytical models, *Ninth AIAA/CEAS Aeroacoustics Conference*, paper 2003-3225, Hilton Head SC, 2003.
[19] A. Fosso-Pouangué, C. Mnasri, S. Moreau, Parameterization and optimization of broadband noise for high-lift devicess, *19th AIAA/CEAS Aeroacoustics Conference*, paper 2013-2065, Berlin, Germany, 2013.
[20] T.F. Brooks, W.M. Humphreys Jr., Flap-edge aeroacoustic measurements and predictions, *Journal of Sound and Vibration* 261 (2003) 31–74.
[21] M. Abramowitz, I. Stegun, *Handbook of Mathematical Functions*, Dover Publications, NY, 1972.
[22] I.S. Gradshteyn, I.M. Ryszik, *Tables of integrals, series and products*, 6th Edition, Academic Press, San Diego, 2000.
[23] M.S. Howe, A review of the theory of trailing-edge noise, *Journal of Sound and Vibration* 61 (1978) 437–465.
[24] C. Bogey, C. Bailly, D. Juvé, Computation of flow noise using source terms in linearized Euler's equations, *AIAA Journal* 40 (2) (2002) 235–243.
[25] A.A. Oberai, F. Roknaldin, T.J.R. Hughes, Computation of trailing-edge noise due to turbulent flow over an airfoil, *AIAA Journal* 40 (11) (2002) 2206–2216.
[26] J.H. Seo, K.W. Chang, Y.J. Moon, Aerodynamic noise prediction for long-span bodies, *12th AIAA/CEAS Aeroacoustics Conference*, Boston MA, 2006.
[27] R.K. Amiet, Acoustic radiation from an airfoil in a turbulent stream, *Journal of Sound and Vibration* 41 (1975) 407–420.
[28] Y.P. Guo, Prediction of flap side-edge noise, *Fifth AIAA/CEAS Aeroacoustics Conference*, paper 1999-1803, Seattle, 1999.
[29] Y.P. Guo, On noise reduction by flap side edge fences, *Journal of Sound and Vibration* 277 (2004) 369–390.
[30] D. Casalino, A. Hazir, E. Fares, B. Duda, M.R. Khorrami, On the connection between flap side-edge noise and tip vortex dynamics, *21st AIAA/CEAS Aeroacoustics Conference*, paper 2015-2992, Dallas, 2015.
[31] P. Mel'nik, Yu.K. Podlipenko, On Green's function for the Helmholtz equation in a wedge, *Ukrainian Mathematical Journal* 45 (9) (1993) 1471–1474.
[32] Virtual Lab Rev 12: User Manual, LMS International, 2012.
[33] W. Desmet, Boundary element modeling for acoustics. *Lecture Notes of the ISAAC21 Course*, K.U.Leuven, Leuven, Belgium, September 2010.
[34] D. Angland, Aerodynamics and Aeroacoustics of Flap Side-Edges, PhD Dissertation, Univ. Southampton, February 2008.
[35] M. Jacob, V. Gradoz, A. Lousiot, D. Juve, S. Guerrand, Sound produced by a backward facing step under a wall jet, *Fourth AIAA/CEAS Aeroacoustics Conference*, paper 1998-2302, Toulouse, France, 1998.
[36] C.L. Streett, Numerical simulation of a flap-edge flow field, *Fourth AIAA/CEAS Aeroacoustics Conference*, paper 1998-2226, Toulouse, France, 1998.
[37] D.S. Jones, *Acoustic and Electromagnetic Waves*, Oxford Univ. Press, 1986.